Micro-mechanical analysis of soil-structure interface behavior under constant normal stiffness condition with DEM

Pei WANG[1], Zhen-Yu YIN[1,*], Wan-Huan ZHOU[2], and Wei-bin CHEN[2]

[1] Department of Civil and Environmental Engineering, The Hong Kong Polytechnic University, Hung Hom, Kowloon, Hong Kong, China

[2] State Key Laboratory of Internet of Things for Smart City and Department of Civil and Environmental Engineering, University of Macau, Macau, China

* Corresponding authors: Dr. Zhen-Yu YIN, Tel: +852 3400 8470; Fax: +852 2334 6389; Email: zhenyu.yin@polyu.edu.hk; zhenyu.yin@gmail.com

Abstract

The mechanical behavior at soil-structure interface (SSI) has a crucial influence on the safety and stability of geotechnical structures. However, the behavior of SSI under constant normal stiffness condition from micro to macro scale receives little attention. In this study, the frictional characteristics of SSI and the associated displacement localization under constant normal stiffness condition are investigated at both macro- and microscales by simulating a series of interface shear tests with discrete element method (DEM). The algorithm to achieve a constant normal stiffness is first developed. The macroscopic mechanical response of the interface shear tests with both loose and dense specimens at various normal stiffness is discussed in terms of shear stress, normal stress, vertical displacement, horizontal displacement and stress ratio. Then the microscopic behaviors and properties, including shear zone formation, localized void ratio, coordination number, force chains and soil fabric are investigated. The effect of normal stiffness is thus clarified at both macro- and microscales.

Keywords soil-structure interface; normal stiffness; micro-mechanical; shear zone; fabric; granular material

Declarations

Funding: GRF project (Grant No. 15217220) and NSFC/RGC Joint Research Scheme (Grant No. N_PolyU534/20) from the Research Grants Council (RGC).

Conflicts of interest/Competing interests: The authors have no conflicts of interest to declare that are relevant to the content of this article.

Availability of data and material: Some or all data and material that support the findings of this study are available from the corresponding author upon reasonable request.

Code availability: Some or all code that support the findings of this study are available from the corresponding author upon reasonable request.

Authors' contributions: Conceptualization: [Pei Wang, Zhen-Yu Yin]; Methodology: [Pei Wang, Zhen-Yu Yin, Wan-Huan Zhou]; Formal analysis and investigation: [Pei Wang, Zhen-Yu Yin, Wei-Bin Chen]; Writing - original draft preparation: [Pei Wang, Zhen-Yu Yin]; Funding acquisition: [Zhen-Yu Yin]

1. Introduction

The behavior of soil-structure interface is important in many situations in geotechnical engineering, such as pile foundations, geosynthetic-reinforced structures, underground structures, off-shore structures, and retaining walls [1-5]. Therefore, a good understanding of the shearing mechanism is essential for geotechnical design and construction. In previous studies, a variety of interface shear tests with different equipment, including direct shear, simple shear, ring shear and large-scale inclined plane shear devices, were conducted to investigate the shear strength and frictional angle of soil-structure interface [6-10]. Specifically, the effects of surface roughness, relative density, dilatancy angle, degree of saturation, particle size, normal stress, loading rate, cyclic load on the shearing behaviors at soil–structure interface were investigated by many researchers [11-20]. Within the framework of continuum mechanics, different constitutive models were proposed to model the interface shear behavior, such as the nonlinear elasticity model, elasto-plasticity model, damage model and two-surface plasticity model [21-26]. In order to numerically simulate the interface behavior, the interface finite element was developed, which includes three ingredients: a contact constraint scheme, a contact discretization method and a constitutive model [27-31]. In recent years, the soil-structure interface was investigated using discrete element method (DEM) to further explain the macroscopic behaviors as well as analyze the failure mechanism at microscale [32-39]. The advantage of using DEM lies in that it can capture the movement and contact of each particle and thus allow us to analyze the fabric evolution and progressive shear localization at the interface on a microscopic level.

In the early research on the soil-structure interface, specimens were usually sheared under the conditions of constant normal stress or constant volume. The condition of constant normal stress is widely used because a constant load is applied at the top of the specimen in traditional experiments such as direct and simple shear tests [12,18,39-41]. The constant volume condition was also adopted in some studies to study the effect of fully restrained volume change. However, in many practical problems, neither the normal stress nor the soil volume remains constant, such as the interface between a pile shaft and the surrounding soil, where the volume change at the interface is constrained by the soil beyond this zone [42]. The normal stiffness, defined by the incremental normal stress over the incremental normal displacement, is a more stable value in such conditions. And the constant normal stress and constant volume conditions are two limiting cases with the normal stiffness respectively equal to zero and infinity [43]. Therefore, by modifying traditional shear devices, the effect of normal stiffness is studied with both monotonic and cyclic shear tests, and the macroscopic interface behaviors and microscopic observations based on particle image velocimetry are presented [42,44-47]. However, previous experimental studies on the soil-structure interface with constant normal stiffness mainly focus on macroscopic behaviors and observations, while ignores the micro-mechanical analysis and micro-mechanism, such as the evolutions of local void ratio, force chains and contact fabric. In terms of numerical analysis with DEM, although the soil-structure interface has been simulated at both 2D and 3D, the general condition of constant normal stiffness has not been investigated. Therefore, in this study, a series of interface shear tests are simulated with DEM at the constant normal stiffness condition. An effective algorithm to achieve the condition of constant normal stiffness is developed. Both loose and dense specimens are generated for simulations. The normal stiffness has a wide range representing different interface conditions. The macroscopic interfacial behaviors are investigated first, and the microscopic properties, including shear zone, global and localized void ratio, coordination number, and soil fabric are also discussed.

It is important to mention that numerical tests in this study are performed using two-dimensional (2D) DEM code PFC2D because a large number of particles raise the problem of calculation efficiency in 3D, particularly in this model with an iterative process. In a previous study, by comparing with the results of 3D simulations, 2D models have been confirmed to be able to predict the qualitative nature of soil particles, although quantitative difference still exists [48]. Some successfully 2D DEM simulations can also be found in [33,34,49,50]. Therefore, although the 2D DEM model was not quantitatively calibrated against with experimental results, it is validated through similar evolution trends of shear stress, normal stress and stress ratio at the macroscale. In addition, a 3D model with the same model parameters is presented in Section 4.3 and yields realistic stress ratios, which indirectly validates the 2D model.

2. DEM simulation

2.1. Sample preparation and soil properties

In order to investigate the behavior of soil-structure interface under constant normal stiffness condition, a series of interface shear tests are simulated using DEM. The DEM was first introduced by Cundall for modeling jointed rock masses in the1970s and now is widely used in simulating the behavior of soils and rocks [51-53].

The schematic diagram of the interface shear test model is shown in Fig. 1. The length (L) and height (H) of the model are respectively 100 mm and 40 mm. The periodic boundary condition is adopted on both sides of the model. Under the periodic boundary condition, when the centroid of a particle falls outside of one side of the boundary, it will be translated back to the opposite side with the same velocity. Therefore, the side walls and the associated boundary effect are eliminated in the simulations. Another advantage of using the periodic boundary condition is the low computational cost which is achieved by reducing the shearing length and number of particles. A sawtooth plate is placed at the bottom of the soil sample, which is made of inclined saw teeth with inclination alternatively equal to 45º and 135º. The surface roughness of the bottom plate is quantified by the parameter R_n, which is defined as R_{max} / D_{50}, where

R_{max} is the absolute vertical distance between the highest peak and lowest valley along with the surface profile over a length equal to D_{50}. To transfer shear localization into the adjacent soil packings [54], a rough surface with R_n equal to 0.7 is used for all simulations. It was reported by Wang and Gutierrez [55] that a minimum value of 40 for H/D_{max} should be used as optimal for direct shear testing. Therefore, the H/D_{max} for interface shear test should be greater than 20 to eliminate the box scale effect. In this study, the height of the sample is chosen as 40 mm so that the value of H/D_{max} is around 50. It is also worthwhile to mention that in order to focus on the effect of normal stiffness, dry sand is used in this study, and the pore pressure and capillary cohesion in unsaturated soils are not considered [56].

Both loose and dense specimens with relative densities ($D_r = (e_{max} - e)/(e_{max} - e_{min})$) of 20% and 80% are simulated in this study, where e_{max}, e_{min} and e are respectively the maximum, minimum and current void ratios of a soil sample. The method proposed by Wood and Maeda [57] is used to determine the e_{max} and e_{min}, in which the loosest and densest samples are generated by setting initial particle friction coefficient and void ratio respectively as 1.0 and 0.3 to get e_{max} and 0.0 and 0.1 for e_{min}. Then with a given relative density, the soil sample is created as follows: (1) the top and sawtooth walls are created with a dimension of 100 mm × 40 mm; (2) the number of soil particles is calculated based on the particle size distribution (PSD) and relative density, and then non-overlapped particles are generated within the domain using the Multi-layer with Undercompaction Method (UCM) [58]; (3) the particle assembly is subjected to a compressive stress of σ_n by moving the top wall towards soil particles. Note that because particles are in disc shape in 2D DEM, it is difficult to prepare a very loose specimen. Therefore, the loose specimen with a relative density of 20% may also experience some dilation during shearing. The minimum and maximum particle diameters are respectively 0.374 mm and 0.781 mm. During the particle generation process, the size range of particles is divided into ten intervals, and the number of particles in each interval is calculated based on the corresponding mean particle size of the interval. Therefore, a quasi-linear PSD is obtained with the average diameter, D_{50}, equal to 0.578 mm. The density of particles is 2650 kg/m^3. The particle interactions are governed by the linear contact model in which the linear elastic frictional behavior for both normal and shear directions is provided. The normal stiffness of both walls and particles is set as 5.0×10^7 N/m according to previous DEM studies [59,60], which ensures small overlaps (less than 1% of average particle diameter) between contacting particles. The ratio of normal and shear stiffness is 2.0, which is within the recommended range for soil particles [61,62]. An empirical value of friction coefficient 0.5 is used for particle-particle contacts according to previous studies [63,64], and a higher value of 0.9 is adopted for particle-wall contacts to ensure that shear localization occurs within the soil zone. In order to numerically account for the effect of particle shape, the rolling resistance method is applied. In this method, an artificial rotational torque is provided at the contact, and its direction is against the direction of the relative rotational increment [65-67]. This method is able to reproduce both macro- and micro-scopic behaviors of slightly elongated granular material when the rolling resistance coefficient is smaller than 0.3 [68-70]. In this study, a low rolling resistance coefficient of 0.1 is adopted to simulate rounded particles with slight elongation according to a series of biaxial tests with DEM conducted by the authors [71]. The model parameters are summarized in Table 1, which were validated in previous DEM studies by the authors [2,34,72].

2.2. Development of constant stiffness control of interface shearing

As discussed in several studies [44,42,45], the condition of constant normal stiffness is likely to prevail in many geotechnical practices such as pile foundations, because any volume change at the interface is constrained by the soils beyond this zone. Therefore, to better understand the soil-structure interfacial behavior under the condition of constant stiffness, a series of interface shear tests are conducted on specimens prepared in previous section.

It was proposed by Boulon and Foray that the normal stiffness of the soil surrounding a pile is given as $k = 4G/d$, where G is the shear modulus of soil and d is the pile diameter. Therefore to consider soils of different types and modulus, the values of constant stiffness are chosen as 0 kPa/mm, 100 kPa/mm, 1000 kPa/mm and 10000 kPa/mm. The shear tests are conducted incrementally in the DEM model, and the following relationship between normal stress increment, $\Delta\sigma_n$, and vertical displacement increment, Δu, is fulfilled in each increment through a back-calculation process.

$$k = \frac{\Delta\sigma_n}{\Delta u} \qquad (1)$$

For a given $\Delta\sigma_n$, the determination of Δu needs special attention because any vertical movement of the loading platen will change the normal stress as well as the normal stiffness of the soil body k_{soil}. As a result, Eq. (1) no longer holds. In order to solve this issue, an iterative process is adopted to calculate Δu in each shear increment, and the flowchart is shown in Fig. 2. At the beginning of each shear increment, a constant shear velocity of 0.1 m/s is applied to the sawtooth wall, and the sample is sheared with a displacement Δd_s equal to 0.01 D_{50}. An increment of normal stress, $\Delta\sigma_n^i$, is generated due to the shear process in this increment. Then the shear is paused and the iterative process to adjust the position of loading platen is initiated. By envisioning the soil sample as a spring with stiffness of k_{soil} working in parallel with the loading spring with a constant stiffness k, the displacement of the loading platen Δu^i is given by

$$\Delta u^i = \frac{\Delta \sigma_n^i}{k + k_{soil}} \quad (2)$$

And the desired normal stress after the vertical movement is $\sigma_n^i + k\Delta u^i$. However, because k_{soil} is not a constant and affected by particle arrangement, the true normal stress after movement, $\sigma_n^{i\prime}$, may not equal to the desired normal stress. If the convergence criterion of constant stiffness is satisfied or the total iterative trials is greater than 20, the model continues to the next shear increment. Otherwise, the iteration is repeated with updated values of σ_n^{i-1} and k_{soil}. The interface shear test stops when the shear displacement reaches 20 D_{50}. It takes about 40 hours on a workstation (Inter Xeon E5-2690A CPU and 128 GB RAM) to simulate one test. The relationships of Δu and $\Delta\sigma_n$ in the interface tests for both loose and dense specimens with various k are shown in Fig. 3 and Fig. 4. As shown in Fig. 3 and Fig. 4, the condition of constant stiffness is successfully maintained in all the interface shear tests. The slight fluctuations in loose specimens with k equal to 0 kPa/mm may come from the convergence issue in a few shear increments, except which the condition of constant normal stiffness is satisfied reasonably well.

3. Results and discussion of interface tests

3.1. Macroscopic behaviors

Fig. 5 shows the shear stress versus shear displacement obtained from DEM simulations and experiments performed on both loose and dense specimens at different normal stiffness. For loose specimens in Fig. 5(a), the increase of the normal stiffness causes a significant reduction of the shear stress. Particularly, the shear stress in the test with $k = 10000$ kPa/mm decreases to zero after a shear displacement of 16 D_{50}, which is due to the detachment of the specimen and the loading platen. Contrary to the loose specimens, the shear stress increases with the increase of the normal stiffness for the dense specimens as shown in Fig. 5(b). When the normal stiffness is low (100 kPa/mm), the shear stress is very close to that in the constant normal stress condition ($k = 0$ kPa/mm). As k continues to increase, the shear stress increases significantly. At the condition of $k = 10000$ kPa/mm, the simulation is stopped much earlier because of the large overlaps induced by the high normal stress at the particle contacts. These large overlaps contradict the small-overlap assumption of DEM and make the simulation results no longer reliable [73]. Compared with the experimental results at similar conditions ($R_n = 0.95$, $k = 0$-1250 kPa/mm) from DeJong and Westgate [43] in Fig. 5(c), the effect of normal stiffness on the shear strength of dense specimens is qualitatively similar, i.e. the shear stress increases with normal stiffness. However, the shear stress also increases with normal stiffness for loose specimens in the experiments, compared with a decreased stress ratio in the DEM simulations (Fig. 5(a)). The seemly opposite results can be explained by the different relative densities in the DEM simulations and experiments. A lower relative density of 20%, compared with 35% in experiments, is adopted in the DEM simulations, which leads to an overall contraction or very slight dilation of the soil specimens. As a result, shear stress decreases with the increase of normal stiffness. In another experimental study with very loose specimens, the interface shear stress is also found to decrease with the increase of normal stiffness [42].

The evolutions of normal stress are presented in Fig. 6. In general, the normal stress decreases with the increase of normal stiffness in tests with loose specimens, and increases for dense specimens. The different evolution trends of the loose specimens in the DEM simulations (Fig. 6(a)) and experiments (Fig. 6(c)) can also be explained by the different initial relative densities and volume changes, similar to the difference for shear stress in Fig. 5. As expressed in Eq. (1), the negative vertical displacement of the loose specimens in DEM simulations leads to a decrease in normal stress. Particularly, the normal stress decreases to zero in the test with $k = 10000$ kPa/mm (close to the undrained constant volume condition) in Fig. 6(a) due to the static liquefaction which refers to the phenomenon that the deviator stress of loose specimens drops significantly under underained/constant volume shearing [74,75]. Besides, due to the lack of controllability (instability of sand) [76,77], the specimen experiences some fluctuation of stability before totally losing it at a shear displacement around 16 D_{50} . The above observations are consistent with the experiment results of the pile skin friction at the condition of constant normal stiffness reported in [42]. It is also noticeable that obvious fluctuations occur in Fig. 5 to Fig. 8, especially those of the loose specimens. In fact, these fluctuations can be attributed to the 2D simulation, and 3D simulations significantly decrease the fluctuations, as shown in Section 4.3. However, these fluctuations don't affect the evolutions of the macroscopic properties, and has only very slight effect on the simulation results.

Fig. 7 shows the evolutions of the vertical displacements of loose and dense specimens during the interface shear tests. During the tests, loose specimens contract at the beginning of the tests and then become dilative, as shown in Fig. 7(a). Due to the low relative density, the total dilation of loose specimens, indicated by the final vertical displacement, is less than 0.5%. The final vertical displacement decreases with the increase of normal stiffness, except for the simulation with $k = 10000$ kPa/mm, which is due to the collapse of the specimen and detachment of the soil from the loading platen. For the dense specimens in Fig. 7(b), soils are always dilative and the magnitudes of dilation are much larger than those of the loose ones. For example, the final vertical displacement is 0.5 mm at a dense state compared to 0.04 mm at a loose state when $k = 100$ kPa/mm. And the vertical displacement decreases with stiffness for dense specimens. The evolution pattern of vertical displacement and the effect of normal stiffness for dense specimens are similar to those in the experiments in Fig. 7(c) [43].

Evolutions of stress ratio (shear stress/normal stress) with respect to normalized shear displacement are shown in Fig. 8. In simulations with loose specimens in Fig. 8(a), the stress ratio increases with shear displacement up to a stable state, similar to the loose specimens in experiments in Fig. 8(c). For the dense specimens, the stress ratio increases much faster than the loose ones until reaching the peak values, after which a softening process can be observed. Results from Fig. 8 also indicate that the evolution of stress ratio is mainly determined by the relative density of soil specimens, and the effect of normal stiffness is very slight. This observation is consistent with the experimental results that the peak stress ratio of uncrushable granular materials is insensative to normal stiffness [45,78]. In the tests by DeJong and Westgate [43], however, it is found that the stress ratio decreases with the increase of normal stiffness for dense specimens, as shown in Fig. 8(c). The exact reason for different observations in above experimental tests is unclear and beyond the scope of this study, but may be explained by the different amount of particle breakage in experiments, which significantly decreases the shear resistance of granular material. This assumption is confirmed by the results of interface shear tests of the sand-woven geotextile interface [79], in which the peak stress ratio of uncrushable glass beads is insensitive to the normal stress, while the ratio of crushable sand decreases with the increase of normal stress. The values of stress ratios at the end of the simulations (residual stress ratios) are around 0.3 for both loose and dense specimens, which can be explained by the constant slope of the failure envelope in the critical state soil mechanics. Using the Mohr-Coulomb equation, the peak and residual friction angles are respectively given as 23.8º and 17.2º. Note that because particles have a lower average coordination number in 2D than that in 3D, both of the two values are smaller than the tested results of sands [43].

3.2. Thickness of the shear and dilation zones

In the interface test, the strain localization arises at the rough surface and gradually develops within the area a few times D_{50} from the surface [80,81]. In the following context, this area will be called the shear zone. Accurate measurement of the thickness of the shear zone is important for theoretical models and continuum-based numerical simulations, in which the thickness of the shear zone should be given as a priori value. In this study, the formation and development of the shear zone are investigated by monitoring the horizontal displacement of particles at different heights. And the thickness is obtained by separating a discrete zone at the interface in which particles have strong displacement localization [82].

In order to investigate the development of displacement localization, the evolution of average normalized shear displacement of soil particles in the interface test with the dense specimen at $k = 1000$ kPa/mm is presented in Fig. 9. The normalized shear displacement is defined as the ratio of particle displacement in the shear direction and the shear displacement of the bottom rough surface (d_s). At the early stages of the shear test ($d_s = 0.3D_{50}$ and $d_s = 1.4D_{50}$ in Fig. 9), only slight displacement localization can be observed at the bottom, and the normalized shear displacement shows a quasi-linear increase across the specimen. At the shear displacement of 3.4 D_{50}, which corresponds to the peak shear stress according to Fig. 5(b), the bending of the curve at the bottom becomes more obvious indicating the initiation of displacement localization. As the interface shear continues to 20.0 D_{50}, the shear displacements of particles almost completely localize at the bottom and a shear zone can be clearly identified. This evolution pattern of shear zone is in good agreement with the experimental observations [82]. Noth that the developments of displacement localization in other tests are similar and therefore not presented here.

The horizontal displacements of particles at the end of interface shear tests are presented in Fig. 10. Particles at the bottom show much larger displacements than the upper ones, and a shear zone with strong strain localization is well-developed in all loose and dense specimens. Above the shear zone, the horizontal displacement gradually decreases to zero as the vertical position increases. The loose specimens have lower strain localization, indicated by larger horizontal displacements of particles above the shear zone. This can be explained by the weaker interlocking among particles in the loose specimens, which provides less contraints no the movement of particles. Similar results were also reported in [83,84]. Slightly different and almost identical horizontal displacements are observed respectively for loose and dense specimens at different normal stiffness in Fig. 10, indicating the low effect of normal stiffness and normal stress on the horizontal displacements of particles. In addition, particles at the bottom have a similar magnitude of horizontal displacements with the shearing platen, i.e. very slight interface sliding. This observation is consistent with previous interface studies with rough surfaces, in which particles are trapped by the roughness and the interface failure is induced by the internal failure of soil particles [43,84].

A simple method to obtain the thickness of the shear zone is proposed and showed in Fig. 11. This method is based on the idea that the boundary of the localization zone is marked by an abrupt change in the displacement gradient. After the interface test, the curvature of the normalized shear displacement versus normalized vertical position curve is calculated, as the red line shown in Fig. 11. The point with the maximum curvature (point A in Fig. 11) and the vertical position of point A can be obtained. The shear zone is defined as the region below this vertical position. As shown in Fig. 11, the shear zone thickness in the test with the dense specimen at $k = 1000$ kPa/mm is 8.29 mm which is equal to 14.2 D_{50}. The thicknesses of the shear zones in the tests with different relative densities and stiffness are summarized in Table 2. For the loose specimens, the thickness of shear zone ranges from 18.5 D_{50} to 20.2 D_{50}, not showing a dependence on the magnitude of normal stiffness. For the dense specimens, the thickness slightly decreases with normal stiffness from 15.0 D_{50} for $k = 0$ kPa/mm to 14.2 D_{50} for $k = 1000$ kPa/mm. In addition, the shear zone thickness decreases as the relative density increases, which is consistent with the observation in Fig. 10 and in previous experimental results [85]. In previous studies, the thickness of shear zone, summarized in Table 3, varies from 1 D_{50} to 25 D_{50} and is affected by many factors such as surface roughness and relative density. The shear zone thickness in this study is within the range of previous studies, and close to the upper bound values at high interface roughness.

The vertical displacements of particles in the simulations are presented in Fig. 12. For the loose specimens, particles close to the interface tend to dilate and reach a maximum vertical displacement at the position of 4 to 9 D_{50} depending on the normal stiffness. The position with maximum vertical displacement divides the soil into two parts, i.e. the dilation zone below this position and the contraction zone above it. Because of the initial loose state, the thickness of the dilation zone is much smaller than that of the contraction zone. For the dense specimens in Fig. 12(b), although the dilation still concentrates near the interface, the thickness of the dilation zone is much larger than the corresponding loose ones. Specifically, the whole specimen dilates in the simulation with $k = 0$ kPa/mm (constant normal stress condition). A similar method based on the maximum curvature is used to determine the dilation zone for the dense specimens. The thickness of dilation zone is summarized in Table 2. The initial relative density plays a more significant role in the thickness of dilation zone, i.e. the thickness increases with the increase of relative density. The normal stiffness indirectly affects the thickness of dilation zone by changing the normal stress, and the thickness is negatively correlated with the normal stress.

3.3. Void ratio

During the interface shear test, the volume of the specimen changes (Fig. 7), which can be attributed to the rearrangement of soil particles. At the same time, the void ratio also varies according to the volume change. In order to understand the mechanism of volume change from the microscopic perspective, the localized void ratio, which is the void ratio in a meso-loop, is investigated. The meso-loops are the polygonal loops that are enclosed by contact branches, as shown in Fig. 13. For each meso-loop, the volume of solid particles, V_S, is obtained by the summation of the areas of circle sectors within the meso-loop. And the volume of the meso-loop, V_T, can be calculated by knowing the positions of all vertices. Therefore, the localized void ratio of the meso-loop is given as $(V_T - V_S)/V_S$.

Fig. 14 shows the localized void ratios of the meso-loops before and after the interface shear test in the dense specimen at $k = 1000$ kPa/mm. In Fig. 14, each circle represents a meso-loop whose center is the same as the sphere. The color and size of a sphere respectively indicate the void ratio and void size of the corresponding meso-loop. Before the interface shear test, the voids are randomly distributed both inside and outside of the shear zone, and no void concentration can be observed (Fig. 14(a)). Although the localized void ratio ranges from 0.1 to over 1.0 in different meso-loops, the void sizes are relatively small. The random void distribution indicates that the specimen is homogeneous. The localized void ratio after the shear test is presented in Fig. 14(b). Outside of the shear zone, small voids are randomly distributed, which is in a similar condition before the shear test. Within the shear zone, however, an obvious concentration of large voids can be identified, indicated by large spheres in Fig. 14(b). Besides the increased void size, the localized void ratios are also higher than those before the test. The above observation confirms that interface shear induces significant changes in terms of void size and localized void ratio for particles within the shear zone, but only has a slight effect outside of the shear zone. Similar results are also observed in other tests and will not be shown here.

The void ratios inside and outside of the shear zone in different tests with various normal stiffness are presented in Fig. 15. For the loose specimens, the void ratios inside the shear zones increase by around 10% at the beginning of the shear tests and then become stable at a shear displacement of 6.8 D_{50}. While the void ratios outside of the shear zone slightly decrease at the beginning and also stabilize at the shear displacement of 6.8 D_{50}. It is interesting to see that the macroscopic shear behaviors, including the shear force, normal force and volumetric strain, also plateau at the shear displacement of 6.8 D_{50} according to Figures from 5 to 7, which exhibits a strong dependence on the microscopic behaviors. The influence of normal stiffness is very slight in tests with loose specimens. For tests with dense specimens, both the void ratios inside and outside of the shear zones increase at first and then become stable. The increase of void ratio inside the shear zone (23% on average) is much higher than that outside of the shear zone (less than 5%). In addition, the value of void ratio decreases with the increase of normal stiffness, which can be attributed to the large normal stress generated during the shear test (Fig. 6).

3.4. Coordination number

The coordination number (inter-particle contact number per particle) is an important parameter describing the packing and micro-structure of granular materials. It is has been proved useful in the analysis of particle breakage, pore size distribution, soil fabric and force chains [2,5,86,60,87]. Fig. 16 shows the evolutions of coordination number in the interface shear tests. Before sharing, the coordination numbers of the loose specimens are around 2.6, compared with 3.5 for the dense specimens. The higher coordination numbers in dense specimens indicate a more compacted state with strong interlocking among particles. In the shear test with loose specimens in Fig. 16(a), both the coordination number inside and outside of the shear zone fluctuate within a small range, and the coordination number outside is always higher than that inside the shear zone. Specimens with larger normal stiffness generally have lower coordination numbers, which can be attributed to the decrease of the normal stress during the shear test. However, contrary to the effect in the loose specimens, a significant increase of final coordination number is induced by increasing the normal stiffness, as shown in Fig. 16 (b). For example, the coordination number inside the shear zone increases from 2.55 to 2.81 when the constant normal stiffness is increased from 0 to 1000 kPa/mm. The increased coordination number in dense specimens can be explained by the high normal stress in the test. It is also noticeable that the coordination number decreases beyond the shear zone at the beginning of shearing, which can be explained by the uniform shear deformation before localization [82]. In summary, despite the huge difference in the normal stiffness, it is actually the normal stress generated during the shear test that determines the coordination number in the soil specimen.

3.5. Force chain and soil fabric

One of the important advantages of DEM analysis is the ability to monitor and track the orientation and force magnitude of particle contacts. The force chains and soil fabric are useful micro-descriptors to understand the macroscopic behavior and to develop multi-scale constitutive models [88-92].

The force chain distribution before and after the shear test in the dense specimen with $k = 1000$ kPa/mm is shown in Fig. 17. Before the test, contacts have a preferential orientation in the vertical direction, which can be explained by the vertical compaction in the sample preparation process. The contact network is dense with a large number of weak contacts, indicating that the applied external force is shared by a large number of particles, i.e. low force concentration. In addition, the particle interlocking is weak and elastic energy among particles is low at this state [70,93]. After the shear test, the initially vertically oriented weak force chains gradually change their preferential orientation to align to the shear direction, as shown in Fig. 17(b). The contact network is dominated by thick force chains. Strong anisotropy and force concentration is generated. Compared with the initial state, the magnitude of the normal contact force also increases significantly.

In order to quantify the evolution of anisotropy and internal structure during the interface shear test, three fabric descriptors are analyzed, i.e. particle contact orientation, normal contact force and shear contact force. For a given contact between two soil particles, the contact orientation is defined as the normalized vector connecting the centroids of the two particles. In a soil specimen, the angular contact orientation distribution, $E(\theta)$, is given by [94]

$$E(\theta)=\frac{1}{2\pi}[1+a\cos 2(\theta-\theta_a)] \quad (3)$$

where a defines the magnitude of anisotropy and θ_a defines the principal direction of anisotropy. In the same way, the normal and shear contact force distributions, $f_n(\theta)$ and $f_s(\theta)$, are respectively expressed as

$$f_n(\theta)=f_{n0}[1+a_n\cos 2(\theta-\theta_n)] \quad (4)$$

and

$$f_s(\theta)=-f_{s0}a_s\sin 2(\theta-\theta_s), \quad (5)$$

where f_{n0} and f_{s0} are the average normal and shear contact forces; a_n and a_s are the anisotropy of normal and shear contact force; and θ_n and θ_s are the principal directions of the normal and shear contact force. For detailed explanations of the three fabric descriptors, please refer to [94].

The fabric evolutions in the dense specimen with $k=1000$ kPa/mm at different shear stages are shown in Fig. 18, in which the black lines represent the data measured in the DEM simulations and red lines are the analytical approximations based on Eq. (3) to (5). For all the fabric descriptors from (a) to (l) in Fig. 18, their distributions can be well captured by the analytical approximations. Before the shear test, the contact orientation and normal contact force concentrate in the vertical direction (Fig. 18(a) and (b)), and the peak shear force is around 45º to the horizontal direction (Fig. 18(c)). The low a and a_n indicate very slight anisotropy in terms of contact orientation and normal contact force. In the shearing process, significant anisotropy is generated, as shown in Fig. 18(d) to (l). In the early shear stage at $0.7D_{50}$, the magnitude of contact orientation anisotropy a is increased from 0.09 to 0.23, and the θ_a changes from 91.0º to 49.5º (Fig. 18(d)). Similarly, the normal and shear contact forces also experience some rotation due to the shear process (Fig. 18(e) and (f)). However, as the shear displacement continues to increase, both the magnitude of anisotropy and principal directions of the three descriptors remain almost constant with very slight fluctuation, as shown in Fig. 18(g) to (l). In other words, after the initial anisotropy induced at the beginning of the test, the soil fabric keeps stable.

The evolutions of anisotropy in terms of contact orientation, normal contact force and shear contact force are summarized in Fig. 19 to Fig. 21. Despite the difference in the relative density (loose versus dense), the initial anisotropies are similar among all the specimens. Once the shear starts, a sudden increase of anisotropy of contact orientation is induced, as shown in Fig. 19(a). The magnitudes of anisotropy in dense specimens quickly reach their peaks and then slightly decrease to the final values. While for the loose specimens, the magnitudes of anisotropy increase much slower and have similar values with dense specimens. Besides the magnitude of anisotropy, the ultimate principal directions of dense specimens also change faster than the loose ones (Fig. 19(b)). The effect of normal stiffness on the anisotropy is negligible in Fig. 19(a) and (b), except for the anisotropy induced by the soil collapse in the test with the dense specimen at $k = 10000$ kPa/mm. The evolution pattern of anisotropy of normal contact force is similar to that of contact orientation, as shown in Fig. 20(a-b). And the difference between the loose and dense specimens can be explained by the magnitude of vertical stress induced during the shear tests, see Fig. 6. In Fig. 21(a), the magnitude of anisotropy of shear contact force remains constant during the shear tests with various constant stiffness, which indicates a constant principal stress ratio. And Fig. 21(b) shows that the rotation of the anisotropy also happens at the early stage of the shear test. Still, the normal stiffness has a slight effect on the anisotropy of shear contact force.

4. Discussions

Besides the normal stiffness, it has been reported that the surface roughness and particle characteristics also have a strong influence on the behavior of soil-structure interface. Therefore, their effects are investigated in this section. In addition, one 3D DEM simulation is conducted and the results are compared with the 2D simulations.

4.1. Effect of surface roughness

Three interface shear tests with R_n respectively equal to 0.3, 0.5 and 0.7 are simulated. Except for the surface roughness, these tests are conducted with the same DEM parameters, sample preparation method, and boundary conditions, as discussed previously in Section 2. A constant normal stiffness of 0 kPa/mm is adopted for the tests. The effect of surface roughness on stress ratio and vertical displacement is shown in Fig. 22. The peak and residual stress ratios, as well as the dilation of the specimens increase with the increase of R_n. These observations are consistent with previous studies with different R_n [84,95]. In addition, as R_n increases from 0.3 to 0.7, the stress softening becomes more significant, as shown in Fig. 22(a). In fact, when the R_n is low, a combination of internal failure and interface failure happens near the interface, which results in an "elastic-perfectly plastic" failure pattern at the macroscale. On the other hand, interface soil shear failure dominates the shear behavior in tests with rough surface (high R_n).This transition of failure mode matches well with the experiments by DeJong and Westgate

[43], in which the “elastic-perfectly plastic” failure pattern is observed for tests with R_n equal to 0.008 and 0.074, while softening behavior is found for rough surface with R_n equal to 0.95.

4.2. Effect of inter-particle friction coefficient

It is well-acknowledged that the interparticle friction (μ) influences the macroscopic shear resistance and friction angle of granular materials. In the interface shear tests in this study, because the interface failure is induced by the internal failure of soil particles, the inter-particle friction coefficient plays a significant role in determining the peak and residual frictional angle. Therefore, the effect of inter-particle friction coefficient is investigated with three interface tests with $k = 100$ kPa/mm and μ ranging from 0.3 to 0.7, and the simulations results are presented in Fig. 23. As expected, both peak and residual stress ratios increase with the increase of μ. The peak/residual friction angles for the tests with μ equal to 0.3, 0.5 and 0.7 are 26.6º/19.3º, 24.0º /17.7º, and 18.8º /14.6º, respectively. Note that the low friction angles are due to 2D condition of the simulations, which will be discussed in the following section. In addition, as shown in Fig. 23(b), the vertical displacement also increases with the increase of μ, which is consistent with previous observations in [96]. At the microscale, the effect of μ on the vertical displacement can be explained by the fact that the self-stability of force chains in a specimen is increased with μ, thus resulting in a more dilative behavior [96].

4.3. 2D versus 3D simulations

In order to investigate the difference between 2D and 3D DEM simulations, one interface test is conducted in 3D. The parameters in Table 2 are used in the 3D case, and the surface roughness and normal stiffness are respectively 0.7 and 0 kPa/mm. The sample preparation method in Section 2.1 is used to prepare a dense specimen. As stated in the Introduction, 3D simulations are much more computationally expensive than the 2D ones because of the increased number of particles and higher degrees of freedom. To reduce the computational cost, the parallel PSD method is adopted, in which the mean particle size is increased by 2 times to 1.156 mm while the shape of the new PSD curve remains the same. With this method, the total number of particles in the 3D DEM simulation is around 100,000.

Fig. 24 compares the shear stress/normal stress ratio and vertical displacement in 2D and 3D simulations. As shown in Fig. 24(a), the evolution trends of 2D and 3D simulations are generally similar, and post-peak softening is observed in both tests. The peak and residual stress ratios in 3D are respectively 0.83 and 0.65, which correspond to peak and residual friction angles of 39.7º and 33.0º. Compared with the angles of 23.8º and 17.2º in 2D, the 3D specimen has much larger shear resistance, even though the same DEM parameters are used. The different shear resistance is also confirmed by the numerical study in [97], in which the peak stress ratios in 3D and 2D are 0.76 and 0.32, respectively. Similarly in some other studies with DEM, low shear strengths and friction angles are observed in 2D than 3D [5,35,84]. This difference can be explained by a lower coordination number in 2D, which imposes less resistance to particle movement at the microscale. As a result, the macroscopic frictional angle is decreased. The dilation in 3D is also more significant than that in 2D (Fig. 24(b)), which is consistent with the observations in [98]. In addition, the 3D simulation significantly decreases the fluctuation of stress ratio compared with the 2D counterparts, as shown in Fig. 24(a). This difference may be attributed to the high self-stability and the low possibility of force chain buckling in 3D.

5. Conclusions

The condition of constant normal stiffness is likely to prevail in many soil-structure interfaces. Therefore, in this study, the soil-structure interface behavior at the condition of constant normal stiffness has been investigated with DEM. Soil-structure interface shear tests with both loose and dense soil specimens under constant normal stiffness condition are simulated. A wide range of normal stiffness from 0 to 10000 kPa/mm has been adopted to account for soils with various stiffness. The micro- and macroscopic mechanical responses of the interface tests have been discussed in detail, and the effect of the magnitude of normal stiffness has been clarified. Conclusions of this study are made as follows:

(1) An effective method has been developed to achieve the constant normal stiffness condition in an interface shear test. In the simulation of a interface shear test, for a given stress increment, the determination of displacement increment is adjusted iteratively based on the normal stress and soil stiffness. With the proposed method, the condition of constant normal stiffness is achieved with a wide range of normal stiffness.

(2) At the macroscale, both interface normal and shear stresses decrease for loose specimens and increase for dense specimens with the increase of normal stiffness. These observations are generally consistent with the experimental results and demonstrate the combined effects of normal stiffness and volumetric strain. Particularly, the normal and shear stress of a loose specimen at high normal stiffness may decrease to zero due to the strong volumetric contraction and static liquefaction. While normal and shear stresses of a dense specimen significantly increase (more than 10 times) at high normal stiffness. In addition, despite the difference in relative density and normal stiffness, the residual stress ratios are always the same.

(3) The thickness of shear zone is around 18 to 20 D_{50} for loose specimens and 14 to 15 D_{50} for dense specimens. Shear zone evolution is observed through the progressive development of displacement localization of soil particles, which includes stages of uniform shear deformation, initiation and growth of shear localization, and stabilized shear zone. The shear zone thickness of loose specimens is not affected by the magnitude of normal stiffness in our case, while the thickness for dense specimens slightly decreases with the increases of normal stiffness.

(4) The thickness of dilation zone is sensitive to the void ratio and normal stiffness. The thickness of dilation zone is 4 to 9 D_{50} for loose specimens, and 17 to 22 D_{50} for dense specimens, highly depending on the initial void ratio. Besides, the thickness of dilation zone is also positively related to the magnitude of normal stress. As a result, the thickness of dilation zone increases/decreases with normal stiffness respectively for loose and dense specimens.

(5) Within the shear zone, the void ratio increases by around 10% and 23% for the loose and dense specimens, respectively. A strong concentration of large voids can be identified from the meso-loops near the interface, which explains the macroscopic dilation. At the same time, the coordination numbers of loose specimens fluctuate within a small range due to the combination effect of shear zone dilation and force chain collapse. The coordination numbers of dense specimens significantly decrease as a result of volumetric dilation. After the formation of a stable shear zone, the void ratio and coordination remain almost constant.

(6) In the interface shear test, strong anisotropy and force concentration are generated. For dense specimens, the magnitude of anisotropy quickly reaches a peak and then decreases to a stable value, corresponding to the macroscopic softening behavior. While for the loose specimens, the magnitude of anisotropy increases much slower and has a similar final value with the dense specimen under the same normal stiffness. The effect of normal stiffness on the anisotropy is very slight.

Acknowledgements

This research was financially supported by the Research Grants Council (RGC) of Hong Kong Special Administrative Region Government (HKSARG) of China (Grant No.: 15217220, N_PolyU534/20).

References

1. Cao S, Xue G, Yilmaz E, Yin Z, Yang F (2020) Utilizing concrete pillars as an environmental mining practice in underground mines. Journal of Cleaner Production 278:123433. doi:https://doi.org/10.1016/j.jclepro.2020.123433

2. Wang P, Yin Z-Y (2020) Micro-mechanical analysis of caisson foundation in sand using DEM. Ocean Eng 203:107240. doi:https://doi.org/10.1016/j.oceaneng.2020.107240

3. Namjoo AM, Toufigh MM, Toufigh V (2019) Experimental investigation of interface behaviour between different types of sand and carbon fibre polymer. Eur J Environ Civ En. doi:https://doi.org/10.1080/19648189.2019.1626290

4. Martinez A, Stutz HH (2019) Rate effects on the interface shear behaviour of normally and overconsolidated clay. Geotechnique 69 (9):801-815. doi:https://doi.org/10.1680/jgeot.17.P.311

5. Yin Z-Y, Wang P, Zhang F (2020) Effect of particle shape on the progressive failure of shield tunnel face in granular soils by coupled FDM-DEM method. Tunn Undergr Sp Tech 100:103394. doi:https://doi.org/10.1016/j.tust.2020.103394

6. Yin ZZ, Zhu H, Xu GH (1995) A Study of Deformation in the Interface between Soil and Concrete. Comput Geotech 17 (1):75-92. doi:https://doi.org/10.1016/0266-352X(95)91303-L

7. Reddy ES, Chapman DN, Sastry VVRN (2000) Direct shear interface test for shaft capacity of piles in sand. Geotech Test J 23 (2):199-205. doi:https://doi.org/10.1520/GTJ11044J

8. Uesugi M, Kishida H, Tsubakihara Y (1989) Friction between sand and steel under repeated loading. Soils Found 29 (3):127-137. doi:https://doi.org/10.3208/sandf1972.29.3_127

9. Yoshimi Y, Kishida T (1981) A ring torsion apparatus for evaluating friction between soil and metal surfaces. Geotech Test J 4 (4):145-152. doi:https://doi.org/10.1520/GTJ10783J

10. Stoltz G, Nicaise S, Veylon G, Poulain D (2020) Determination of geomembrane - protective geotextile friction angle: An insight into the shear rate effect. Geotext Geomembranes 48 (2):176-189. doi:https://doi.org/10.1016/j.geotexmem.2019.11.007

11. Rowe PW (1962) The stress-dilatancy relation for static equilibrium of an assembly of particles in contact. Proceedings of the Royal Society of London Series A Mathematical and Physical Sciences 269 (1339):500-527

12. Su LJ, Zhou WH, Chen WB, Jie XX (2018) Effects of relative roughness and mean particle size on the shear strength of sand-steel interface. Measurement 122:339-346. doi:10.1016/j.measurement.2018.03.003

13. Tiwari B, Al-Adhadh AR (2014) Influence of relative density on static soil–structure frictional resistance of dry and saturated sand. Geotechnical and Geological Engineering 32 (2):411-427

14. Wang ZG, Richwien W (2002) A study of soil-reinforcement interface friction. J Geotech Geoenviron 128 (1):92-94. doi:Doi 10.1061/(Asce)1090-0241(2002)128:1(92)

15. Potyondy JGJG (1961) Skin friction between various soils and construction materials. 11 (4):339-353

16. Eid HT, Amarasinghe RS, Rabie KH, Wijewickreme D (2015) Residual shear strength of fine-grained soils and soil-solid interfaces at low effective normal stresses. Can Geotech J 52 (2):198-210. doi:10.1139/cgj-2014-0019

17. Kuo M, Bolton M (2014) Shear tests on deep-ocean clay crust from the Gulf of Guinea. Geotechnique 64 (4):249-257. doi:10.1680/geot.13.P.020

18. Liu SH, Sun DA, Matsuoka H (2005) On the interface friction in direct shear test. Comput Geotech 32 (5):317-325. doi:https://doi.org/10.1016/j.compgeo.2005.05.002

19. Hamid TB, Miller GA (2009) Shear strength of unsaturated soil interfaces. Can Geotech J 46 (5):595-606. doi:10.1139/T09-002

20. Hossain MA, Yin JH (2015) Dilatancy and Strength of an Unsaturated Soil-Cement Interface in Direct Shear Tests. Int J Geomech 15 (5). doi:10.1061/(Asce)Gm.1943-5622.0000428
21. Gomez JE, Filz GM, Ebeling RM (2003) Extended hyperbolic model for sand-to-concrete interfaces. J Geotech Geoenviron 129 (11):993-1000. doi:10.1061/(Asce)1090-0241(2003)129:11(993)
22. Liu HB, Song EX, Ling HI (2006) Constitutive modeling of soil-structure interface through the concept of critical state soil mechanics. Mech Res Commun 33 (4):515-531. doi:10.1016/j.mechrescom.2006.01.002
23. Zeghal M, Edil TB (2002) Soil structure interaction analysis: modeling the interface. Can Geotech J 39 (3):620-628. doi:10.1139/T02-016
24. Zhang G, Zhang JM (2008) Unified modeling of monotonic and cyclic behavior of interface between structure and gravelly soil. Soils Found 48 (2):231-245. doi:DOI 10.3208/sandf.48.231
25. Zaman MM-u, Desai CS, Drumm EC (1984) Interface model for dynamic soil-structure interaction. Journal of Geotechnical Engineering 110 (9):1257-1273
26. Lashkari A, Kadivar M (2016) A constitutive model for unsaturated soil–structure interfaces. Int J Numer Anal Met 40 (2):207-234
27. Cerfontaine B, Dieudonné AC, Radu JP, Collin F, Charlier R (2015) 3D zero-thickness coupled interface finite element: Formulation and application. Comput Geotech 69:124-140. doi:https://doi.org/10.1016/j.compgeo.2015.04.016
28. Zaman Md Mu, Desai Chandrakant S, Drumm Eric C (1984) Interface Model for Dynamic Soil‐Structure Interaction. Journal of Geotechnical Engineering 110 (9):1257-1273. doi:10.1061/(ASCE)0733-9410(1984)110:9(1257)
29. Segurado J, Llorca J (2004) A new three-dimensional interface finite element to simulate fracture in composites. Int J Solids Struct 41 (11):2977-2993. doi:https://doi.org/10.1016/j.ijsolstr.2004.01.007
30. Dolbow J, Harari I (2009) An efficient finite element method for embedded interface problems. Int J Numer Meth Eng 78 (2):229-252. doi:https://doi.org/10.1002/nme.2486
31. Yang J, Yin Z-Y (2021) Soil-structure interface modeling with the nonlinear incremental approach. Int J Numer Anal Met n/a (n/a). doi:https://doi.org/10.1002/nag.3206
32. Jensen RP, Bosscher PJ, Plesha ME, Edil TB (1999) DEM simulation of granular media-structure interface: Effects of surface roughness and particle shape. Int J Numer Anal Met 23 (6):531-547. doi:https://doi.org/10.1002/(SICI)1096-9853(199905)23:6%3C531::AID-NAG980%3E3.0.CO;2-V
33. Wang JF, Gutierrez MS, Dove JE (2007) Numerical studies of shear banding in interface shear tests using a new strain calculation method. Int J Numer Anal Met 31 (12):1349-1366. doi:https://doi.org/10.1002/nag.589
34. Zhu HX, Zhou WH, Yin ZY (2018) Deformation mechanism of strain localization in 2D numerical interface tests. Acta Geotech 13 (3):557-573. doi:https://doi.org/10.1007/s11440-017-0561-1
35. Zhu HX, Zhou WH, Jing XY, Yin ZY (2019) Observations on fabric evolution to a common micromechanical state at the soil-structure interface. Int J Numer Anal Met 43 (15):2449-2470. doi:https://doi.org/10.1002/nag.2989
36. Feng S-J, Chen J-N, Chen H-X, Liu X, Zhao T, Zhou A (2020) Analysis of sand–woven geotextile interface shear behavior using discrete element method (DEM). Can Geotech J 57 (3):433-447. doi:https://doi.org/10.1139/cgj-2018-0703
37. Wang J, Jiang M (2011) Unified soil behavior of interface shear test and direct shear test under the influence of lower moving boundaries. Granul Matter 13 (5):631-641.

doi:https://doi.org/10.1007/s10035-011-0275-2
38. Asadzadeh M, Soroush A (2016) Fundamental investigation of constant stress simple shear test using DEM. Powder Technol 292:129-139. doi:https://doi.org/10.1016/j.powtec.2016.01.029
39. Ji K, Arson C (2020) Tensile strength of calcite/HMWM and silica/HMWM interfaces: A Molecular Dynamics analysis. Constr Build Mater 251:118925. doi:https://doi.org/10.1016/j.conbuildmat.2020.118925
40. Wang HL, Zhou WH, Yin ZY, Jie XX (2019) Effect of Grain Size Distribution of Sandy Soil on Shearing Behaviors at Soil-Structure Interface. J Mater Civil Eng 31 (10). doi:10.1061/(Asce)Mt.1943-5533.0002880
41. Boukpeti N, White DJ (2017) Interface shear box tests for assessing axial pipe-soil resistance. Geotechnique 67 (1):18-30. doi:10.1680/jgeot.15.P.112
42. Tabucanon JT, Airey DW, Poulos HG (1995) Pile Skin Friction in Sands from Constant Normal Stiffness Tests. Geotech Test J 18 (3):350-364. doi:https://doi.org/10.1520/GTJ11004J
43. DeJong JT, Westgate ZJ (2009) Role of Initial State, Material Properties, and Confinement Condition on Local and Global Soil-Structure Interface Behavior. J Geotech Geoenviron 135 (11):1646-1660. doi:10.1061/(Asce)1090-0241(2009)135:11(1646)
44. Ooi LH, Carter JP (1987) A constant normal stiffness direct shear device for static and cyclic loading. Geotech Test J 10 (1):3-12. doi:https://doi.org/10.1520/GTJ10132J
45. Porcino D, Fioravante V, Ghionna VN, Pedroni S (2003) Interface behavior of sands from constant normal stiffness direct shear tests. Geotech Test J 26 (3):289-301. doi:https://doi.org/10.1520/GTJ11308J
46. DeJong JT, Randolph MF, White DJ (2003) Interface load transfer degradation during cyclic loading: A microscale investigation. Soils Found 43 (4):81-93. doi:DOI 10.3208/sandf.43.4_81
47. DeJong JT, White DJ, Randolph MF (2006) Microscale Observation and Modeling of Soil-Structure Interface Behavior Using Particle Image Velocimetry. Soils Found 46 (1):15-28. doi:https://doi.org/10.3208/sandf.46.15
48. Owen PJ, Cleary PW, Mériaux C (2009) Quasi-static fall of planar granular columns: comparison of 2D and 3D discrete element modelling with laboratory experiments. Geomechanics and Geoengineering 4 (1):55-77. doi:10.1080/17486020902767388
49. Khabazian M, Mirghasemi AA, Bayesteh H (2018) Compressibility of montmorillonite/kaolinite mixtures in consolidation testing using discrete element method. Comput Geotech 104:271-280. doi:https://doi.org/10.1016/j.compgeo.2018.09.005
50. Suchorzewski J, Tejchman J, Nitka M, Bobinski J (2019) Meso-scale analyses of size effect in brittle materials using DEM. Granul Matter 21 (1). doi:https://doi.org/10.1007/s10035-018-0862-6
51. Cundall PA A computer model for simulating progressive, large-scale movement in blocky rock system. In: Proceedings of the International Symposium on Rock Mechanics, 1971.
52. Zhang F, Li M, Peng M, Chen C, Zhang L (2019) Three-dimensional DEM modeling of the stress–strain behavior for the gap-graded soils subjected to internal erosion. Acta Geotech 14 (2):487-503. doi:https://doi.org/10.1007/s11440-018-0655-4
53. Zhang J, Wang X, Yin Z-Y, Liang Z (2020) DEM modeling of large-scale triaxial test of rock clasts considering realistic particle shapes and flexible membrane boundary. Eng Geol 279:105871. doi:https://doi.org/10.1016/j.enggeo.2020.105871
54. Frost JD, DeJong JT, Recalde M (2002) Shear failure behavior of granular-continuum interfaces. Eng Fract Mech 69 (17):2029-2048. doi:Doi 10.1016/S0013-7944(02)00075-9
55. Wang J, Gutierrez M (2010) Discrete element simulations of direct shear specimen scale effects. Geotechnique 60 (5):395-409. doi:https://doi.org/10.1680/geot.2010.60.5.395
56. Liu X, Zhou A, Shen S-l, Li J, Sheng D (2020) A micro-mechanical model for unsaturated

soils based on DEM. Computer Methods in Applied Mechanics and Engineering 368:113183. doi:https://doi.org/10.1016/j.cma.2020.113183
57. Wood DM, Maeda K (2008) Changing grading of soil: effect on critical states. Acta Geotech 3 (1):3-14. doi:https://doi.org/10.1007/s11440-007-0041-0
58. Jiang MJ, Konrad JM, Leroueil S (2003) An efficient technique for generating homogeneous specimens for DEM studies. Comput Geotech 30 (7):579-597. doi:https://doi.org/10.1016/S0266-352X(03)00064-8
59. Wu MM, Wang JF (2020) A DEM investigation on crushing of sand particles containing intrinsic flaws. Soils Found 60 (2):562-572. doi:10.1016/j.sandf.2020.03.007
60. Zhao SW, Zhang N, Zhou XW, Zhang L (2017) Particle shape effects on fabric of granular random packing. Powder Technol 310:175-186. doi:https://doi.org/10.1016/j.powtec.2016.12.094
61. Goldenberg C, Goldhirsch I (2005) Friction enhances elasticity in granular solids. Nature 435 (7039):188-191
62. Potyondy DO, Cundall PA (2004) A bonded-particle model for rock. Int J Rock Mech Min 41 (8):1329-1364. doi:https://doi.org/10.1016/j.ijrmms.2004.09.011
63. Wang P, Arson C (2016) Discrete element modeling of shielding and size effects during single particle crushing. Comput Geotech 78:227-236. doi:https://doi.org/10.1016/j.compgeo.2016.04.003
64. Shi JS, Guo PJ (2018) Induced fabric anisotropy of granular materials in biaxial tests along imposed strain paths. Soils Found 58 (2):249-263. doi:10.1016/j.sandf.2018.02.001
65. Ai J, Chen JF, Rotter JM, Ooi JY (2011) Assessment of rolling resistance models in discrete element simulations. Powder Technol 206 (3):269-282. doi:https://doi.org/10.1016/j.powtec.2010.09.030
66. Jiang MJ, Yu HS, Harris D (2005) A novel discrete model for granular material incorporating rolling resistance. Comput Geotech 32 (5):340-357. doi:https://doi.org/10.1016/j.compgeo.2005.05.001
67. Wang X, Gong J, An A, Zhang K, Nie Z (2019) Random generation of convex granule packing based on weighted Voronoi tessellation and cubic-polynomial-curve fitting. Comput Geotech 113:103088. doi:https://doi.org/10.1016/j.compgeo.2019.05.003
68. Zhao SW, Evans TM, Zhou XW (2018) Shear-induced anisotropy of granular materials with rolling resistance and particle shape effects. Int J Solids Struct 150:268-281. doi:10.1016/j.ijsolstr.2018.06.024
69. Liu YM, Liu HB, Mao HJ (2018) The influence of rolling resistance on the stress-dilatancy and fabric anisotropy of granular materials. Granul Matter 20 (1). doi:10.1007/s10035-017-0780-z
70. Barnett N, Rahman MM, Karim MR, Nguyen HBK Evaluating the particle rolling effect on the characteristic features of granular material under the critical state soil mechanics framework. In: Granular Matter, 2020. vol 4. Springer, pp 1-24. doi:https://doi.org/10.1007/s10035-020-01055-5
71. Yin Z-Y, Wang P (2021) Micro-mechanical analysis of caisson foundation in sand using DEM: Particle shape effect. Appl Ocean Res 111:102630. doi:https://doi.org/10.1016/j.apor.2021.102630
72. Wang P, Yin Z-Y (2020) Micro-mechanical analysis of caisson foundation in sand using DEM: Particle breakage effect. Ocean Eng 215:107921. doi:https://doi.org/10.1016/j.oceaneng.2020.107921
73. Huang X, O'Sullivan C, Hanley KJ, Kwok CY (2014) Discrete-element method analysis of the state parameter. Geotechnique 64 (12):954-965. doi:https://doi.org/10.1680/geot.14.P.013
74. Md. Mizanur R, Lo SR (2012) Predicting the Onset of Static Liquefaction of Loose Sand with Fines. J Geotech Geoenviron 138 (8):1037-1041. doi:10.1061/(ASCE)GT.1943-

5606.0000661
75. Yamamuro JA, Lade PV (1997) Static liquefaction of very loose sands. Can Geotech J 34 (6):905-917. doi:10.1139/t97-057
76. Chang CS, Yin ZY, Hicher PY (2011) Micromechanical Analysis for Interparticle and Assembly Instability of Sand. J Eng Mech 137 (3):155-168. doi:10.1061/(Asce)Em.1943-7889.0000204
77. Daouadji A, Darve F, Al Gali H, Hicher PY, Laouafa F, Lignon S, Nicot F, Nova R, Pinheiro M, Prunier F, Sibille L, Wan R (2011) Diffuse failure in geomaterials: Experiments, theory and modelling. Int J Numer Anal Met 35 (16):1731-1773. doi:https://doi.org/10.1002/nag.975
78. Evgin E, Fakharian K (1996) Effect of stress paths on the behaviour of sand-steel interfaces. Can Geotech J 33 (6):853-865. doi:DOI 10.1139/t96-116-336
79. Afzali-Nejad A, Lashkari A, Shourijeh PT (2017) Influence of particle shape on the shear strength and dilation of sand-woven geotextile interfaces. Geotext Geomembranes 45 (1):54-66. doi:10.1016/j.geotexmem.2016.07.005
80. Alshibli KA, Sture S (2000) Shear band formation in plane strain experiments of sand. J Geotech Geoenviron 126 (6):495-503. doi:https://doi.org/10.1061/(Asce)1090-0241(2000)126:6(495)
81. Wiebicke M, Ando E, Viggiani G, Herle I (2020) Measuring the evolution of contact fabric in shear bands with X-ray tomography. Acta Geotech 15 (1):79-93. doi:https://doi.org/10.1007/s11440-019-00869-9
82. Sadrekarimi A, Olson SM (2010) Shear Band Formation Observed in Ring Shear Tests on Sandy Soils. J Geotech Geoenviron 136 (2):366-375. doi:https://doi.org/10.1061/(Asce)Gt.1943-5606.0000220
83. Gu XQ, Chen YW, Huang MS (2017) Critical state shear behavior of the soil-structure interface determined by discrete element modeling. Particuology 35:68-77. doi:10.1016/j.partic.2017.02.002
84. Jing XY, Zhou WH, Zhu HX, Yin ZY, Li YM (2018) Analysis of soil-structural interface behavior using three-dimensional DEM simulations. Int J Numer Anal Met 42 (2):339-357. doi:https://doi.org/10.1002/nag.2745
85. Grabowski A, Nitka M, Tejchman J (2021) 3D DEM simulations of monotonic interface behaviour between cohesionless sand and rigid wall of different roughness. Acta Geotech 16 (4):1001-1026. doi:10.1007/s11440-020-01085-6
86. Gao ZW, Zhao JD (2013) Strain localization and fabric evolution in sand. Int J Solids Struct 50 (22-23):3634-3648. doi:https://doi.org/10.1016/j.ijsolstr.2013.07.005
87. Wang G, Wei JT (2016) Microstructure evolution of granular soils in cyclic mobility and post-liquefaction process. Granul Matter 18 (3). doi:https://doi.org/10.1007/s10035-016-0621-5
88. Yin ZY, Chang CS, Hicher PY (2010) Micromechanical modelling for effect of inherent anisotropy on cyclic behaviour of sand. Int J Solids Struct 47 (14-15):1933-1951. doi:https://doi.org/10.1016/j.ijsolstr.2010.03.028
89. Yin ZY, Xu Q, Chang CS (2013) Modeling Cyclic Behavior of Clay by Micromechanical Approach. J Eng Mech 139 (9):1305-1309. doi:https://doi.org/10.1061/(ASCE)EM.1943-7889.0000516
90. Yin Z-Y, Xu Q, Hicher P-Y (2013) A simple critical-state-based double-yield-surface model for clay behavior under complex loading. Acta Geotech 8 (5):509-523. doi:https://doi.org/10.1007/s11440-013-0206-y
91. Xiong H, Nicot F, Yin ZY (2019) From micro scale to boundary value problem: using a micromechanically based model. Acta Geotech 14 (5):1307-1323. doi:https://doi.org/10.1007/s11440-018-0717-7

92. He X, Wu W, Cai G, Qi J, Kim JR, Zhang D, Jiang M (2020) Work–energy analysis of granular assemblies validates and calibrates a constitutive model. Granul Matter 22 (1):28. doi:10.1007/s10035-019-0990-7
93. Wang P, Arson C (2018) Energy distribution during the quasi-static confined comminution of granular materials. Acta Geotech 13 (5):1075-1083. doi:https://doi.org/10.1007/s11440-017-0622-5
94. Rothenburg L, Bathurst RJ (1989) Analytical Study of Induced Anisotropy in Idealized Granular-Materials. Geotechnique 39 (4):601-614. doi:https://doi.org/10.1680/geot.1989.39.4.601
95. Hu LM, Pu JL (2004) Testing and modeling of soil-structure interface. J Geotech Geoenviron 130 (8):851-860. doi:10.1061/(Asce)1090-0241(2004)130:8(851)
96. Huang X, Hanley KJ, O'Sullivan C, Kwok CY (2014) Exploring the influence of interparticle friction on critical state behaviour using DEM. Int J Numer Anal Met 38 (12):1276-1297. doi:https://doi.org/10.1002/nag.2259
97. Cheung G, O'Sullivan C (2008) Effective simulation of flexible lateral boundaries in two- and three-dimensional DEM simulations. Particuology 6 (6):483-500. doi:10.1016/j.partic.2008.07.018
98. Fleischmann JA, Plesha ME, Drugan WJ (2013) Quantitative Comparison of Two-Dimensional and Three-Dimensional Discrete-Element Simulations of Nominally Two-Dimensional Shear Flow. Int J Geomech 13 (3):205-212. doi:10.1061/(ASCE)GM.1943-5622.0000202
99. Sadrekarimi A, Olson Scott M (2010) Shear Band Formation Observed in Ring Shear Tests on Sandy Soils. J Geotech Geoenviron 136 (2):366-375. doi:10.1061/(ASCE)GT.1943-5606.0000220
100. Iwashita K, Oda M (1998) Rolling Resistance at Contacts in Simulation of Shear Band Development by DEM. J Eng Mech 124 (3):285-292. doi:10.1061/(ASCE)0733-9399(1998)124:3(285)
101. Uesugi M, Kishida H, Tsubakihara Y (1988) Behavior of sand particles in sand-steel friction. Soils Found 28 (1):107-118. doi:https://doi.org/10.3208/sandf1972.28.107
102. Rui S, Wang L, Guo Z, Cheng X, Wu B (2021) Monotonic behavior of interface shear between carbonate sands and steel. Acta Geotech 16 (1):167-187. doi:10.1007/s11440-020-00987-9
103. Chen W-B, Zhou W-H, dos Santos JA (2020) Analysis of consistent soil–structure interface response in multi–directional shear tests by discrete element modeling. Transportation Geotechnics 24:100379. doi:https://doi.org/10.1016/j.trgeo.2020.100379
104. Ho TYK, Jardine RJ, Anh-Minh N (2011) Large-displacement interface shear between steel and granular media. Geotechnique 61 (3):221-234. doi:https://doi.org/10.1680/geot.8.P.086
105. Zhao C, Zhang R, Zhao C, Wang W, Wang Y (2019) A Three-Dimensional Evaluation of Interface Shear Behavior between Granular Material and Rough Surface. J Test Eval 49 (2):713-727. doi:10.1520/JTE20180749
106. Vangla P, Latha GM (2015) Influence of Particle Size on the Friction and Interfacial Shear Strength of Sands of Similar Morphology. Int J Geosynth Groun 1 (1):6. doi:10.1007/s40891-014-0008-9

Table 1 Parameters in DEM simulations

Parameter	Value
Density ρ (kg/m^3)	2650
Normal stiffness of particle k_n^p (N/m)	5.0×10^7
Shear stiffness of particle k_s^p (N/m)	2.5×10^7
Normal stiffness of wall k_n^w (N/m)	5.0×10^7
Shear stiffness of wall k_s^w (N/m)	2.5×10^7
Particle-particle friction coefficient μ (–)	0.5
Particle-wall friction coefficient μ_w (–)	0.9
Rolling resistance coefficient μ_r (–)	0.1
Compressive stress σ_n (kPa)	100
Damping coefficient	0.1

Table 2 Thickness of shear and dilation zones

Specimens		0 kPa/mm	100 kPa/mm	1000 kPa/mm	10000 kPa/mm
Loose	Shear zone	19.8 D_{50}	18.5 D_{50}	20.2 D_{50}	19.7 D_{50}
	Dilation zone	4.4 D_{50}	4.4 D_{50}	6.6 D_{50}	8.8 D_{50}
Dense	Shear zone	15.0 D_{50}	14.4 D_{50}	14.2 D_{50}	-
	Dilation zone	22.3 D_{50}	20.3 D_{50}	17.1 D_{50}	-

Table 3 A summary of shear zone thickness in previous studies

Reference	Shear zone thickness/ D_{50}	Test method
Sadrekarimi and Olson [99]	10-14	Interface ring shear test
Iwashita and Oda[100]	10	2D DEM simulation
Uesugi *et al.* [101]	3-4	Sand-steel interface tests
Gu *et al.* [83]	8-10	2D DEM simulation
Grabowski *et al.* [85]	1-14	3D DEM simulation
Rui *et al.* [102]	1-14	Interface ring shear test
Chen *et al.* [103]	4.0-4.2	3D DEM simulation
Ho *et al.* [104]	4-13	Sand-steel interface test
Zhao *et al.* [105]	8-14	Sand-steel interface test
Vangla and Latha [106]	5-25	Sand-geomembrane interface test

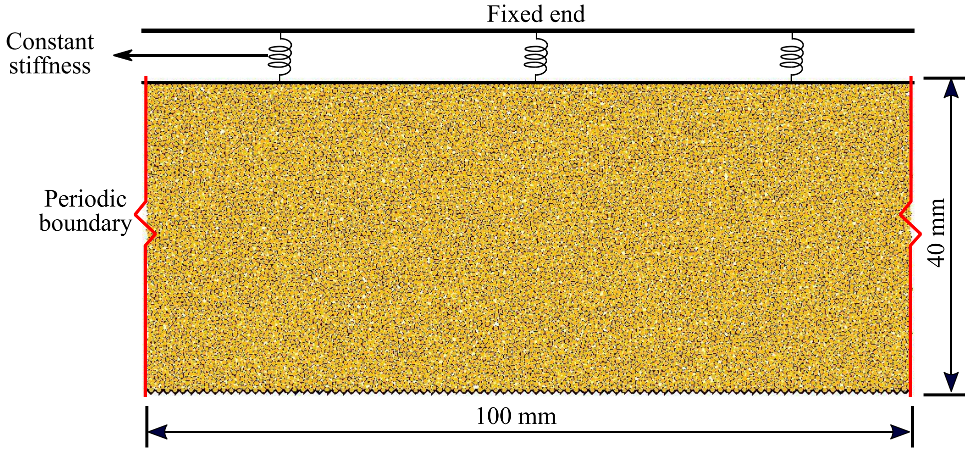

Fig. 1 Schematic diagram of the DEM model

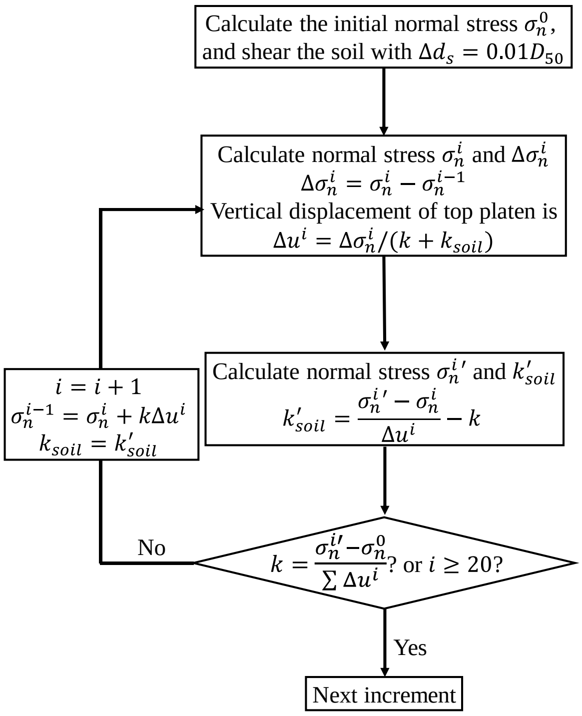

Fig. 2 Flowchart of the shear increment to achieve constant normal stiffness

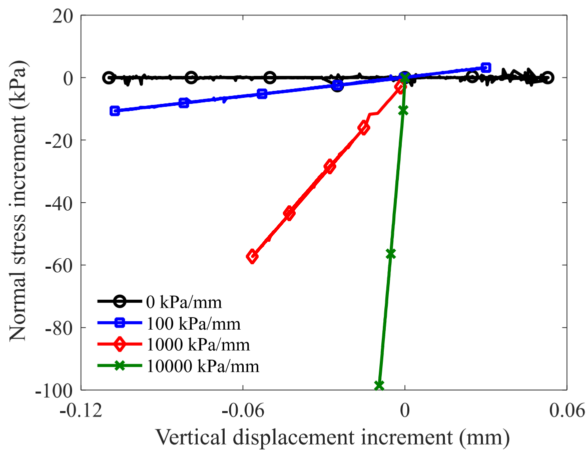

Fig. 3 Vertical displacement increment versus normal stress increment in the interface shear tests of loose specimens with different constant normal stiffness

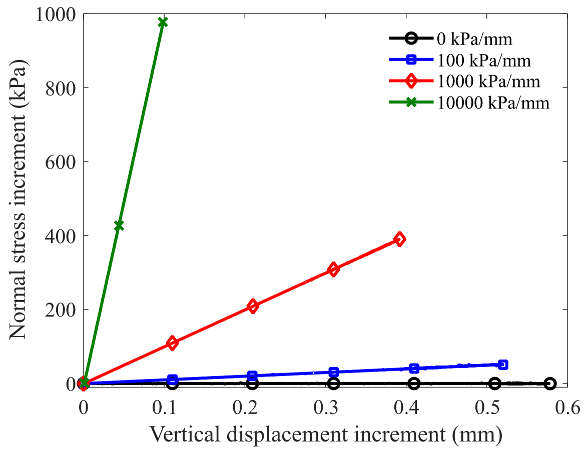

Fig. 4 Vertical displacement increment versus normal stress increment in the interface shear tests of dense specimens with different constant normal stiffness

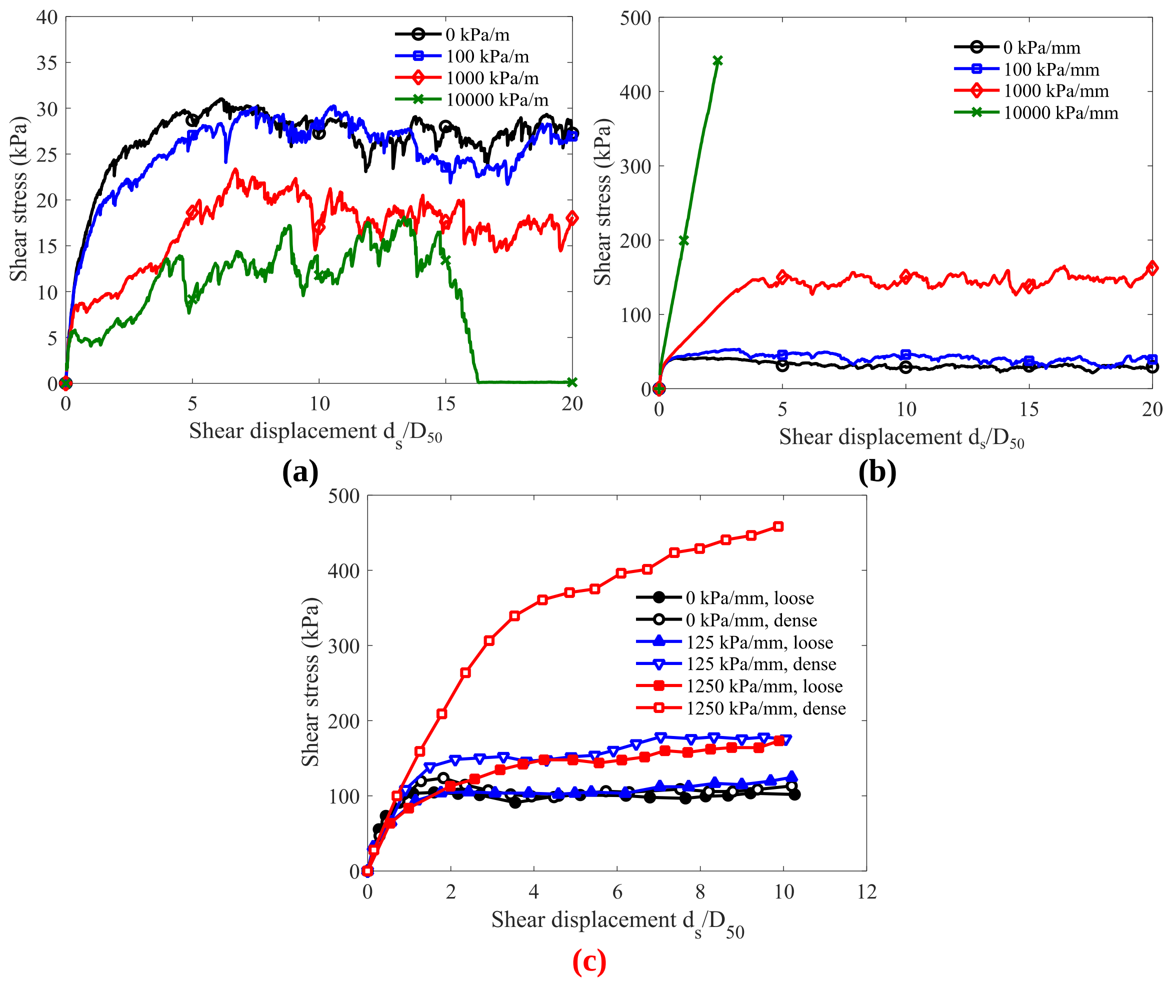

Fig. 5 Shear stress versus shear displacement of interface shear tests with different normal stiffness: (a) DEM simulations with loose specimens; (b) DEM simulations with dense specimens; and (c) experiments [43]

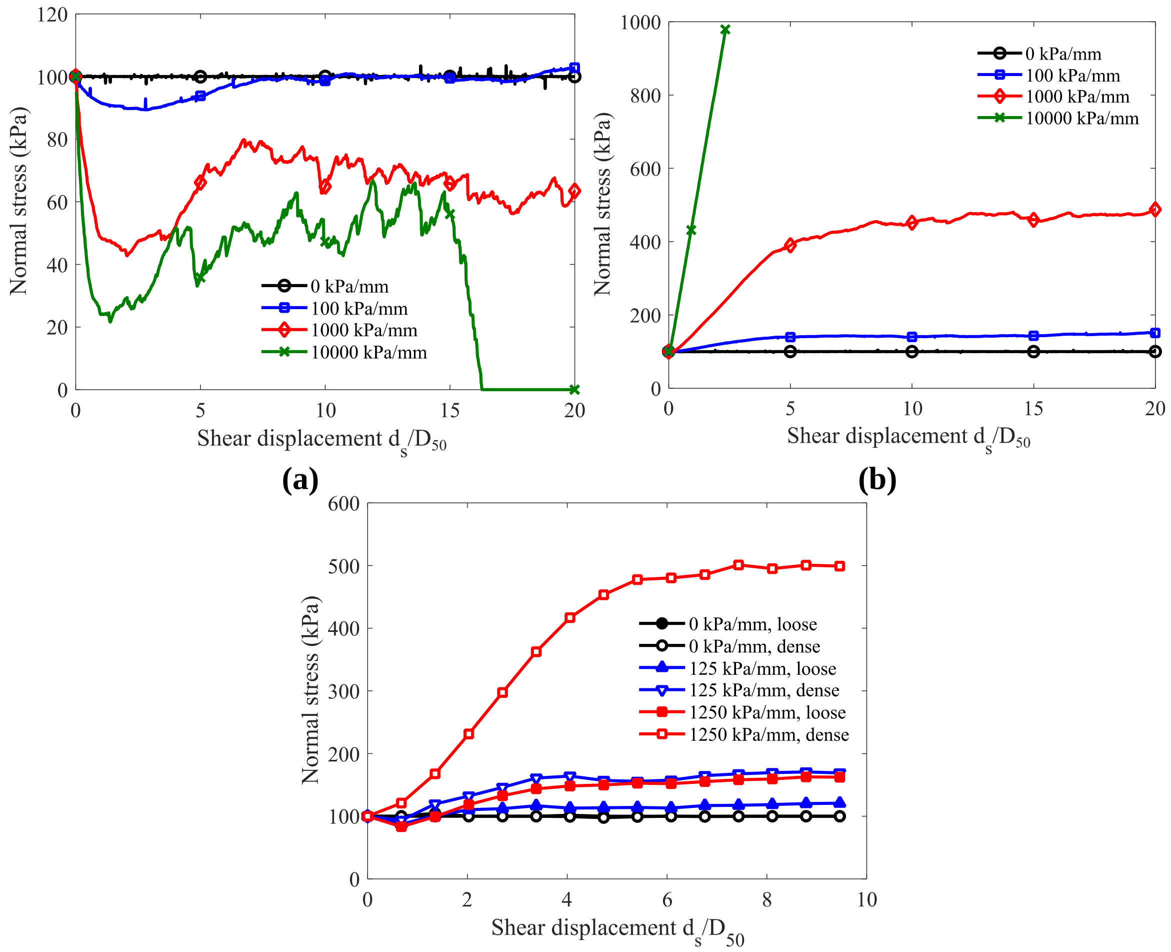

(c)

Fig. 6 Normal stress versus shear displacement of interface shear tests with different normal stiffness: (a) DEM simulations with loose specimens; (b) DEM simulations with dense specimens; and (c) experiments [43]

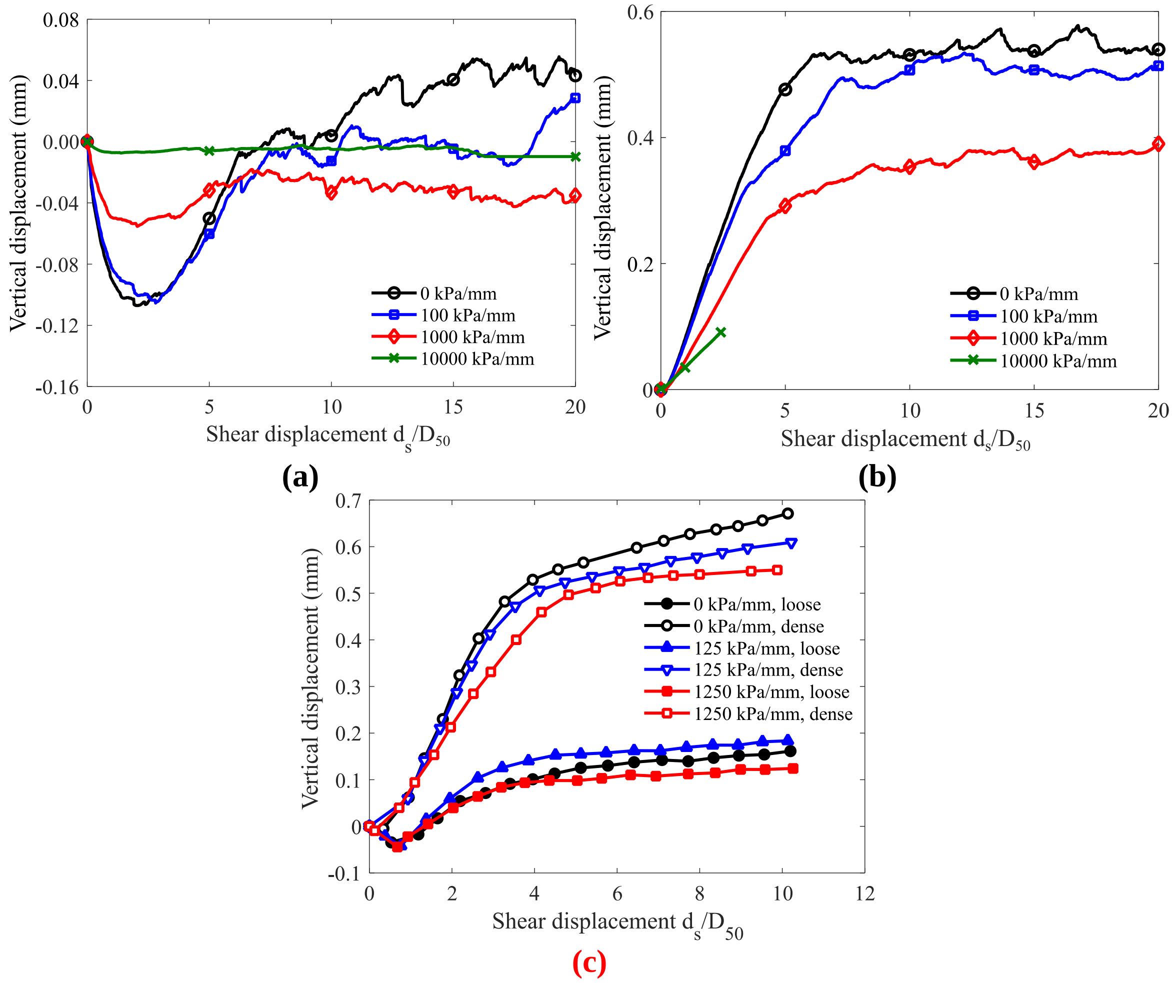

Fig. 7 Vertical displacement versus shear displacement of interface shear tests with different normal stiffness: (a) DEM simulations with loose specimens; (b) DEM simulations with dense specimens; and (c) experiments [43]

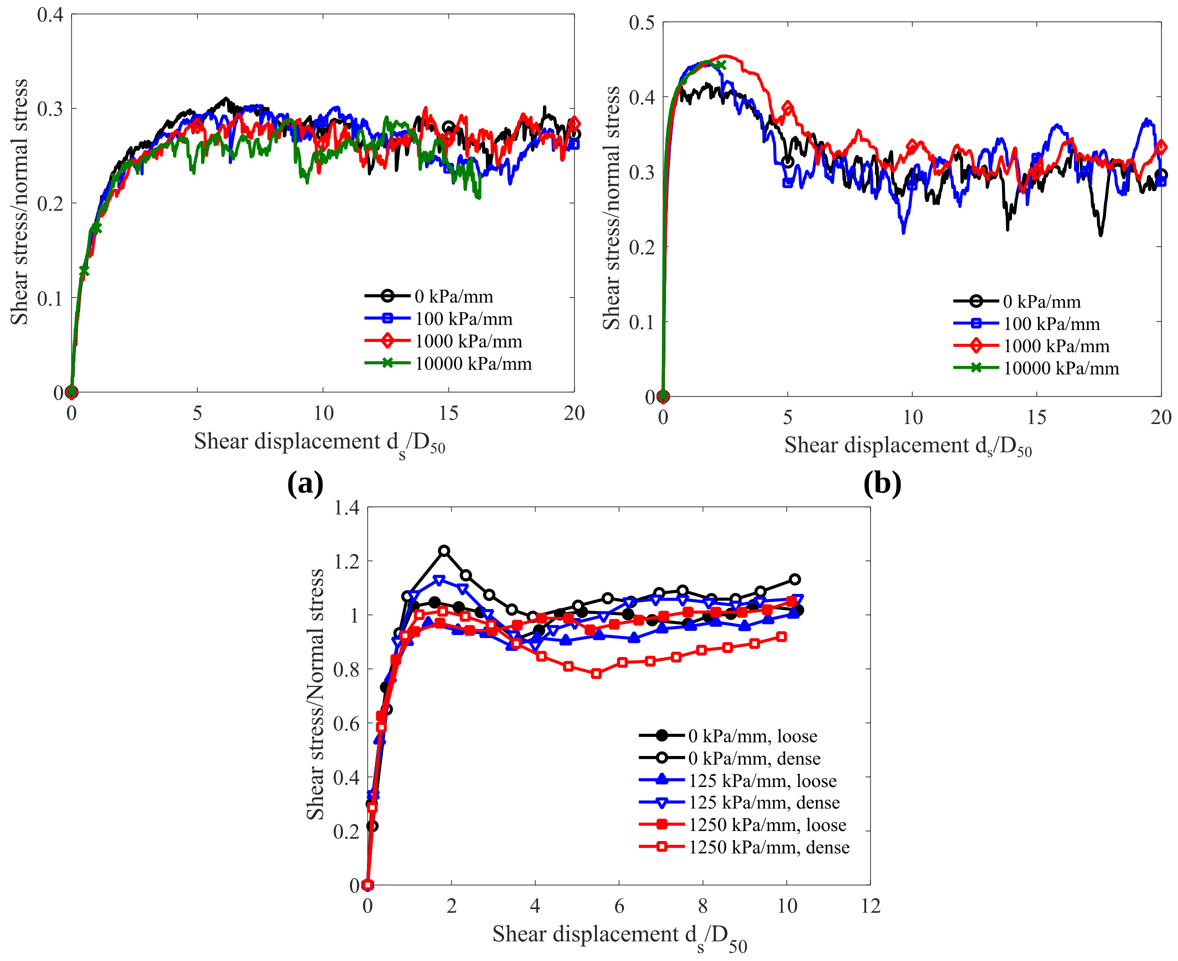

Fig. 8 Shear stress/normal stress versus shear displacement of interface shear tests with different normal stiffness: (a) DEM simulations with loose specimens; (b) DEM simulations with dense specimens; and (c) experiments [43]

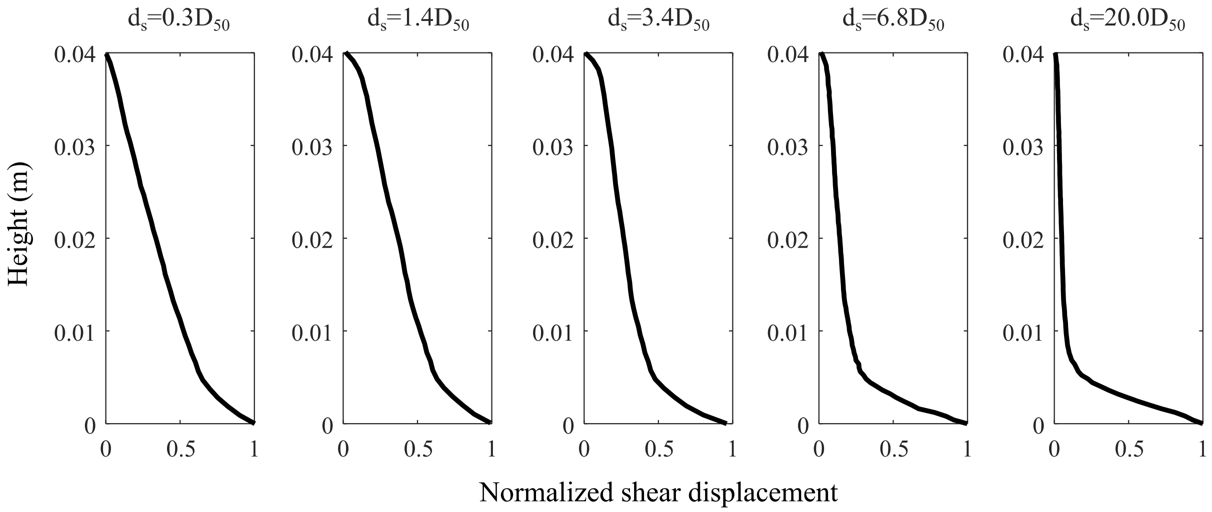

Fig. 9 Average normalized displacement of particles in dense specimen with $k = 1000$ kPa/mm at different shear displacements

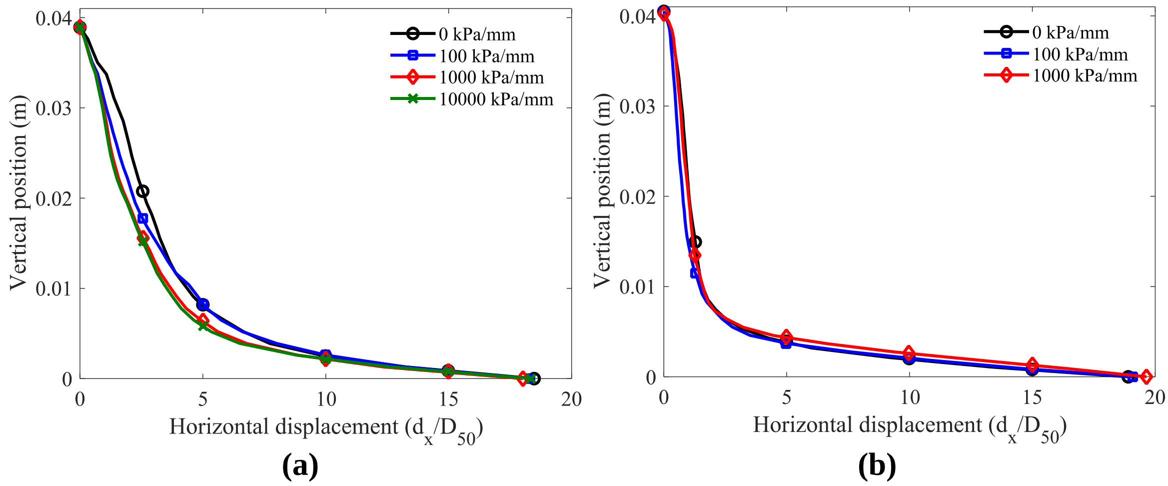

Fig. 10 Horizontal displacement of particles from simulations of interface shear tests with different constant stiffness: (a) loose specimen and (b) dense specimen

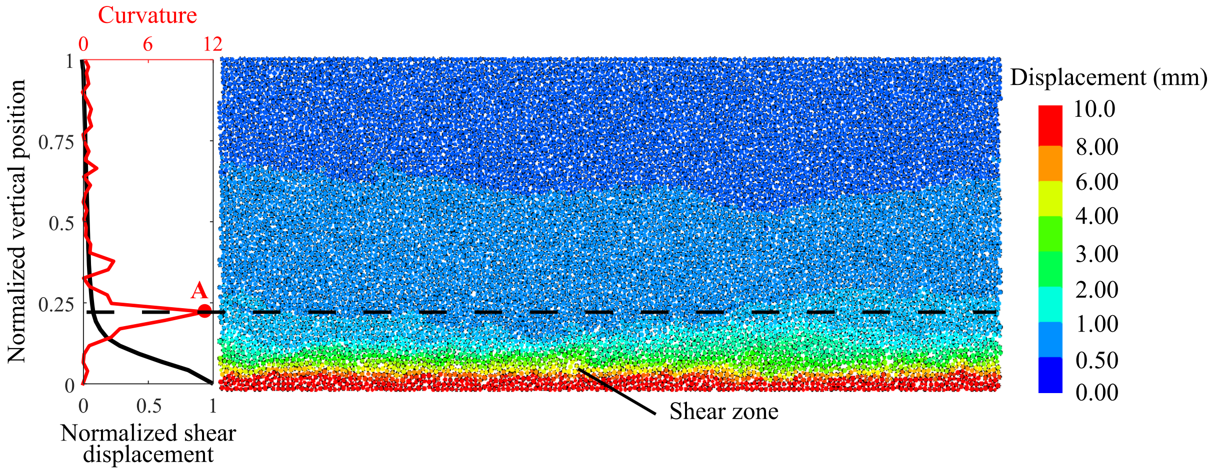

Fig. 11 Determination of the shear zone thickness in the interface shear test

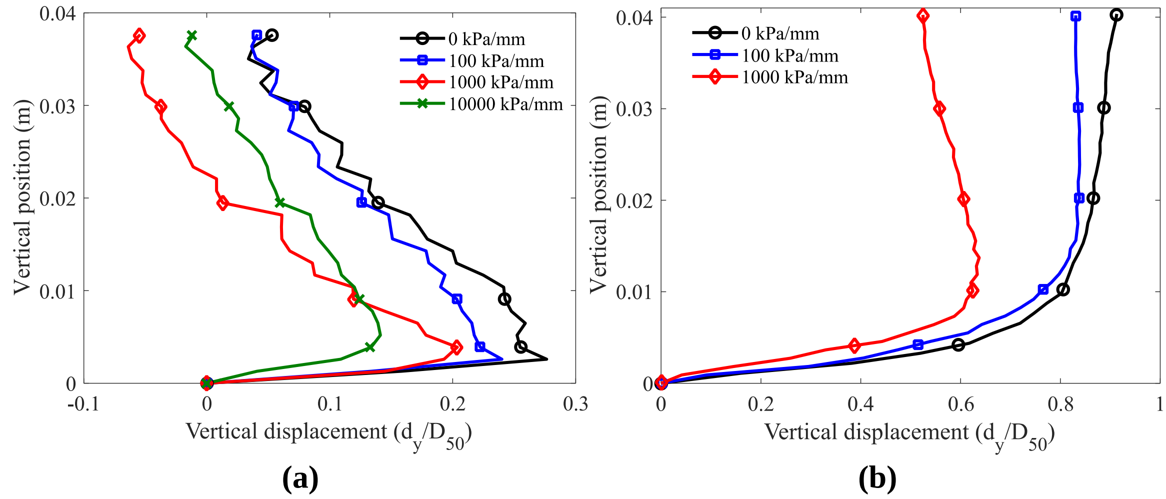

Fig. 12 Vertical displacement of particles from simulations of interface shear tests with different constant stiffness: (a) loose specimen and (b) dense specimen

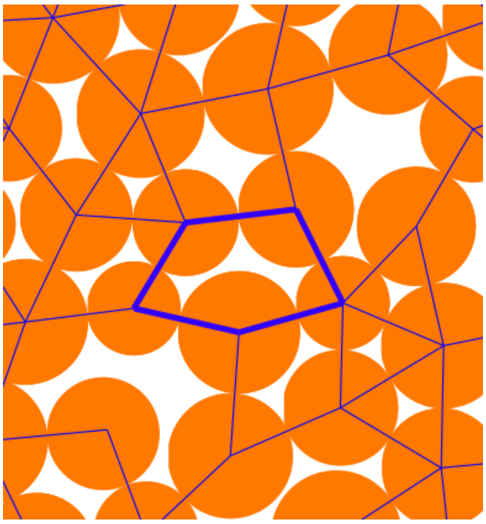

Fig. 13 Polygonal meso-loops enclosed by contact branches

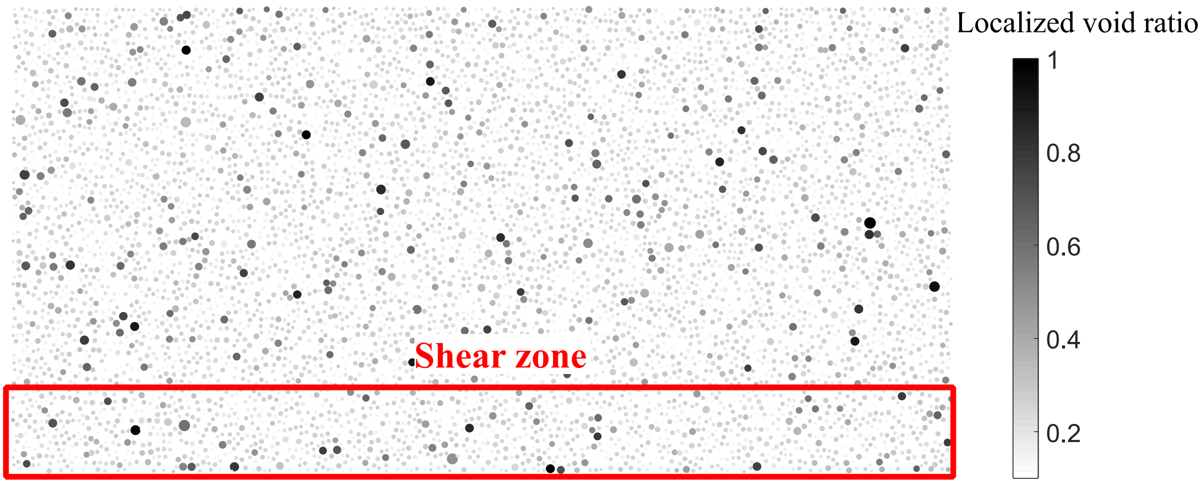

(a)

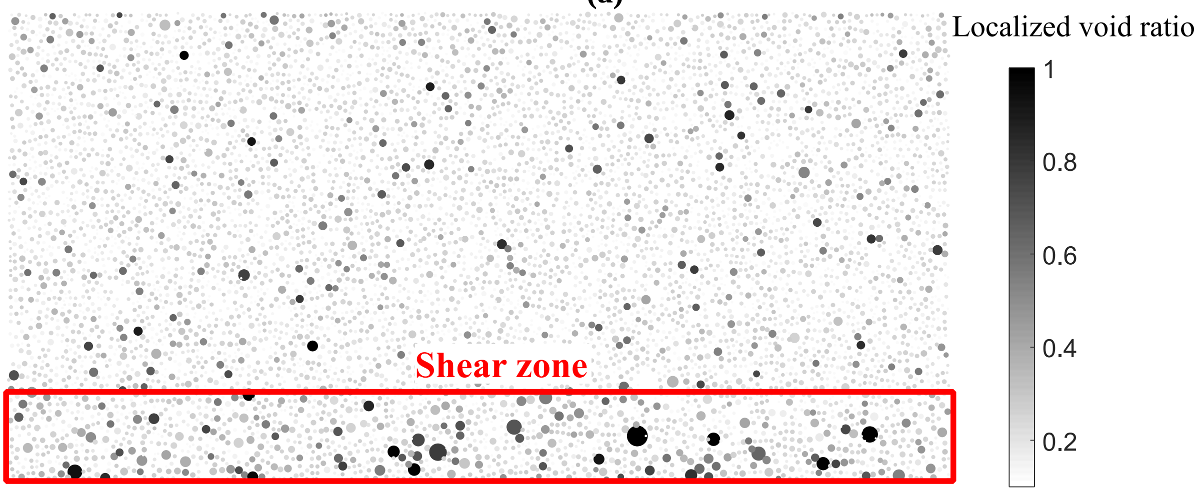

(b)

Fig. 14 Localized void ratios of the meso-loops in dense specimen with $k = 1000$ kPa/mm before (a) and after (b) shear test

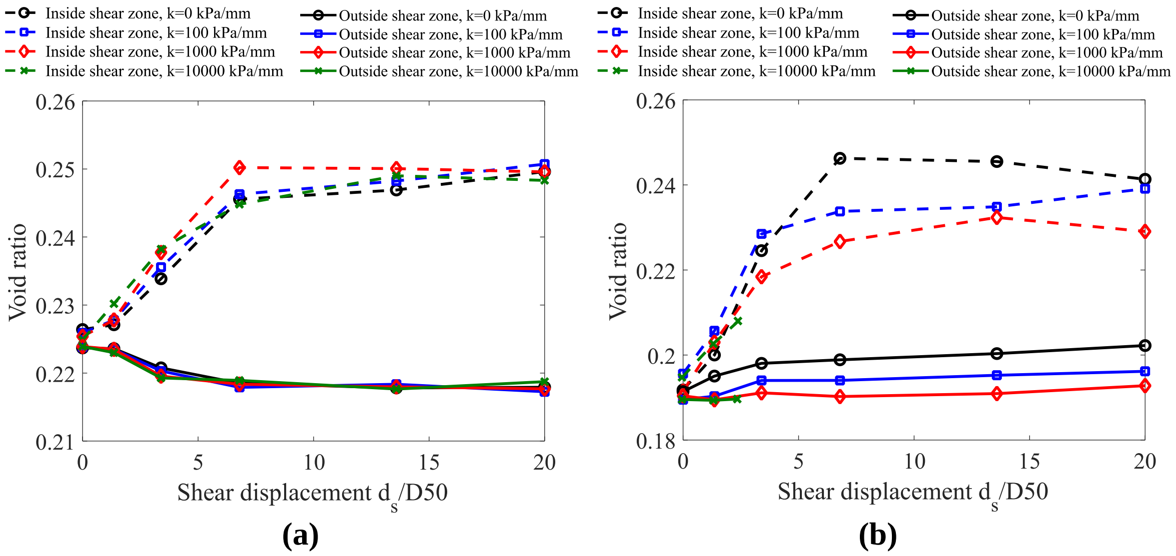

Fig. 15 Evolution of void ratio inside and outside of shear zone in interface shear test with (a) loose specimens and (b) dense specimens

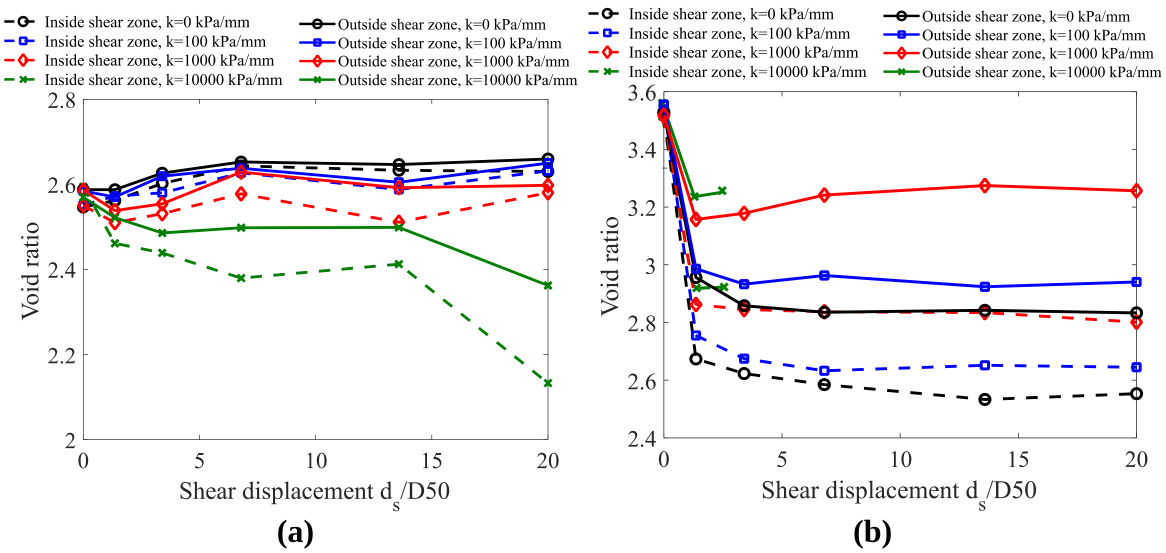

Fig. 16 Evolution of coordination number inside and outside of shear zone during interface shear test from (a) loose specimens and (b) dense specimens

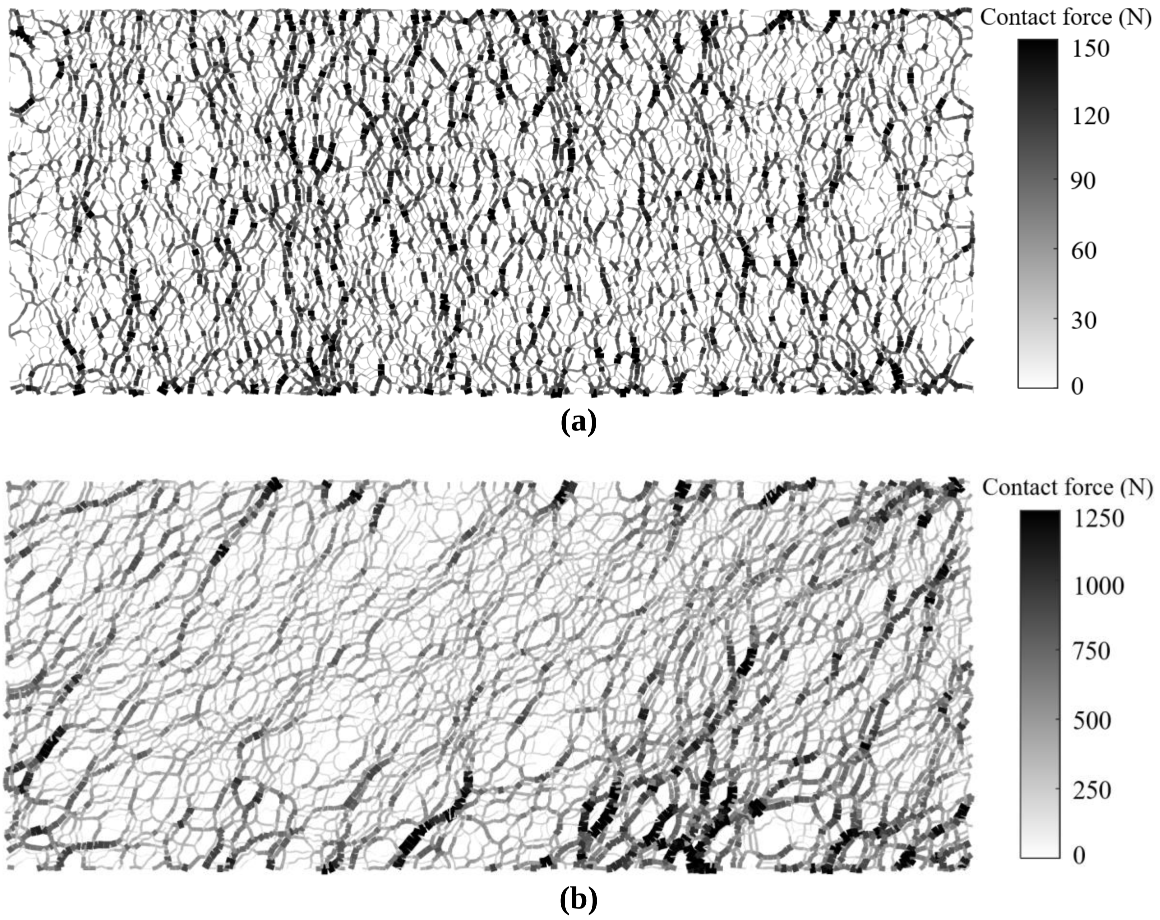

Fig. 17 Force chain distribution in dense specimen with $k = 1000$ kPa/mm before (a) and after (b) interface shear test

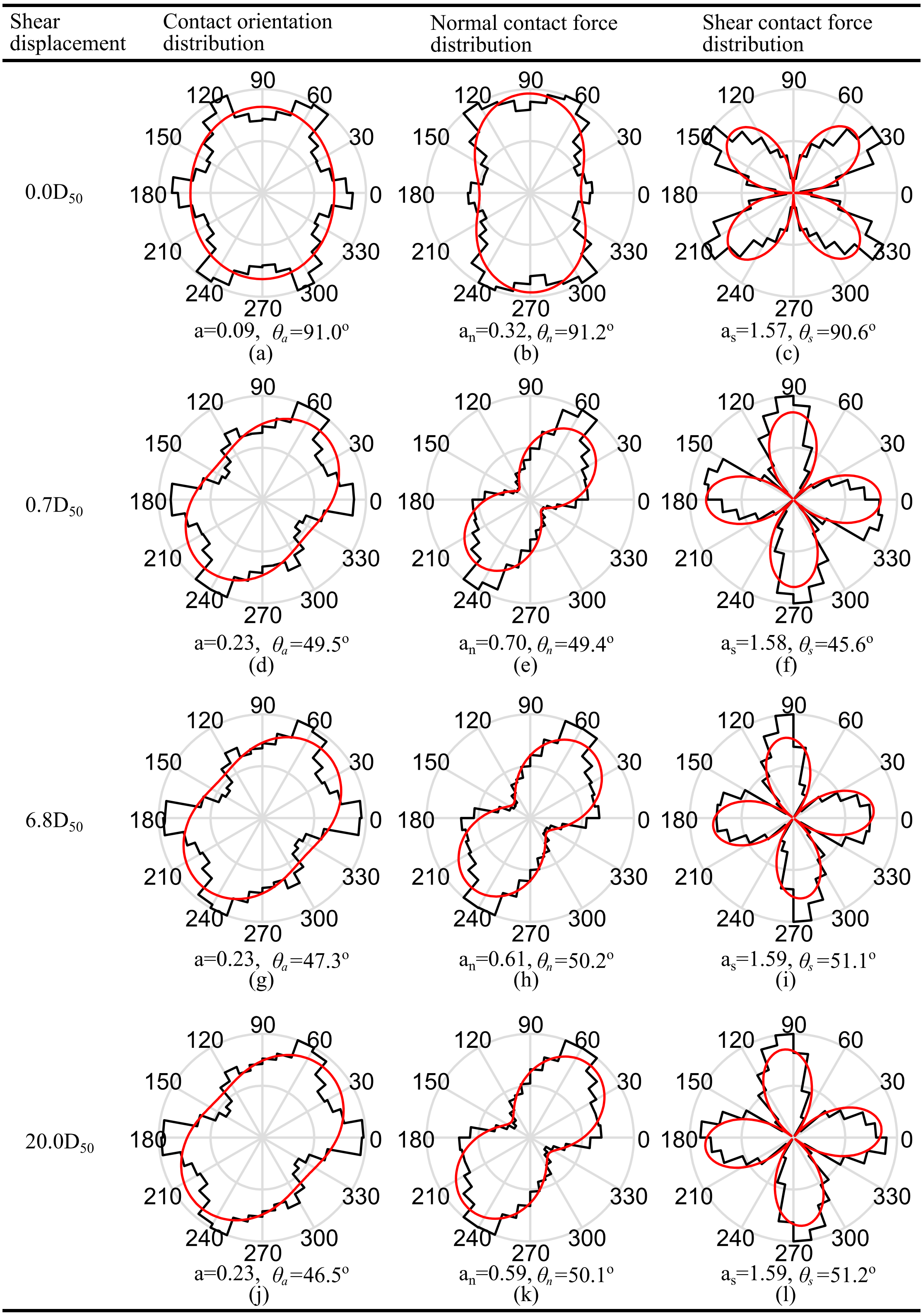

Fig. 18 Fabric evolution of particles in dense specimen with $k = 1000$ kPa/mm

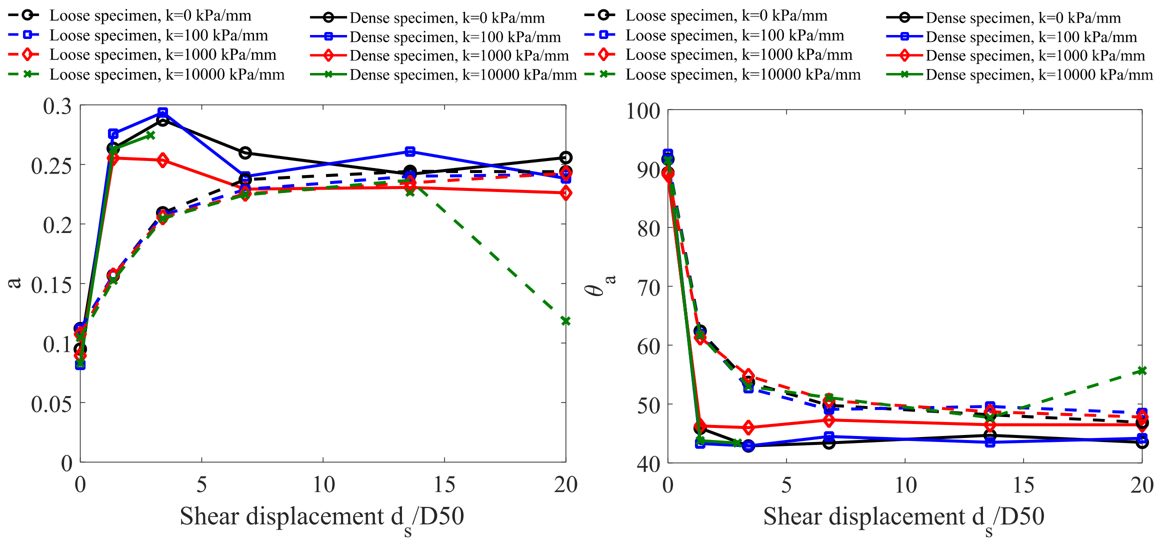

(a) (b)

Fig. 19 Evolution of anisotropy of contact orientation in interface shear tests: (a) magnitude of anisotropy; (b) principal direction of anisotropy

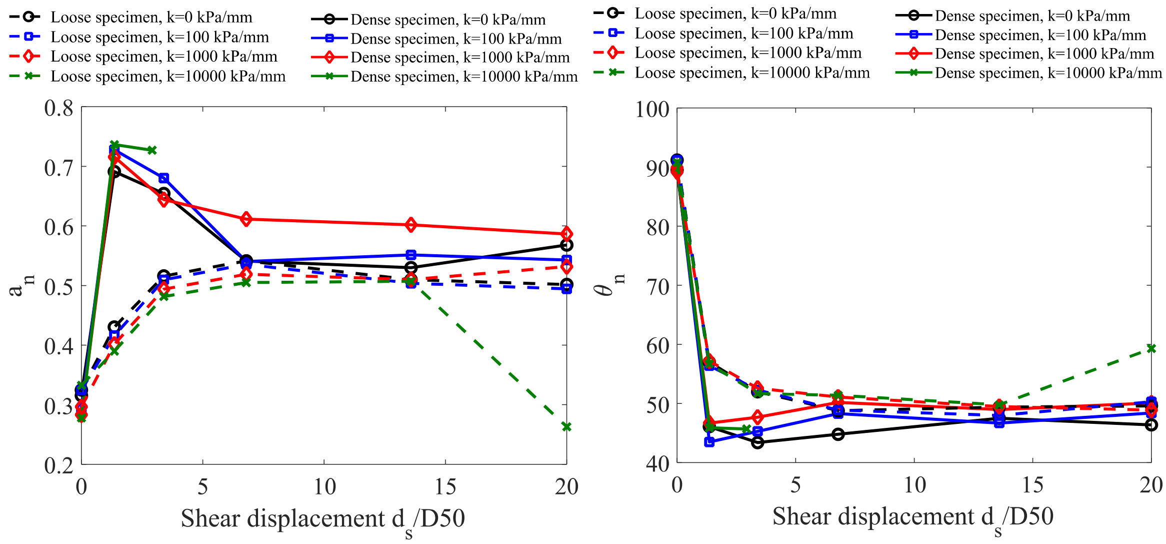

(a) (b)

Fig. 20 Evolution of anisotropy of normal contact force in interface shear tests: (a) magnitude of anisotropy; (b) principal direction of anisotropy

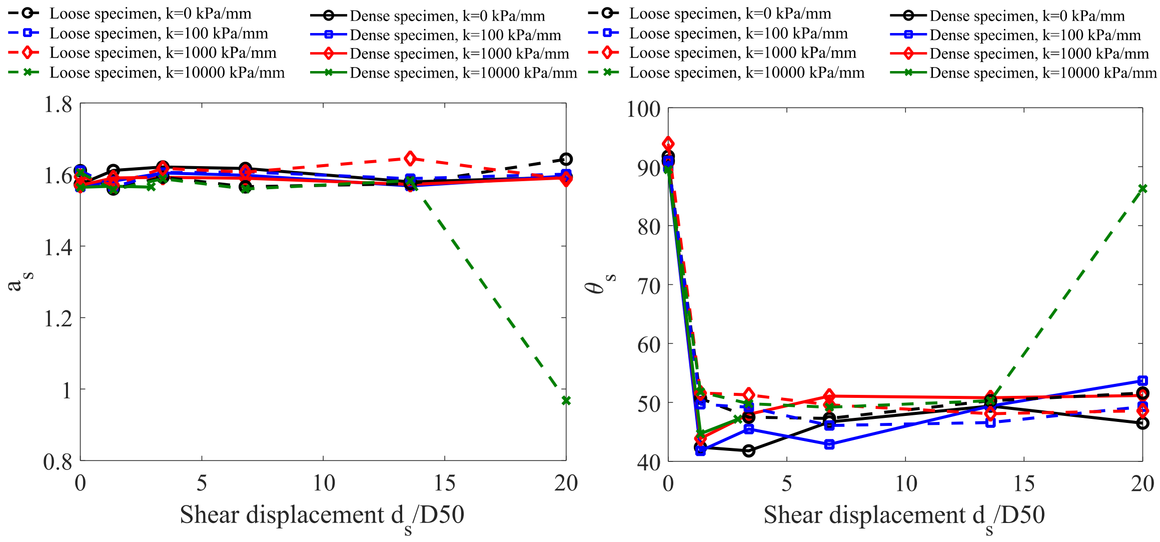

(a) **(b)**

Fig. 21 Evolution of anisotropy of shear contact force in interface shear tests: (a) magnitude of anisotropy; (b) principal direction of anisotropy

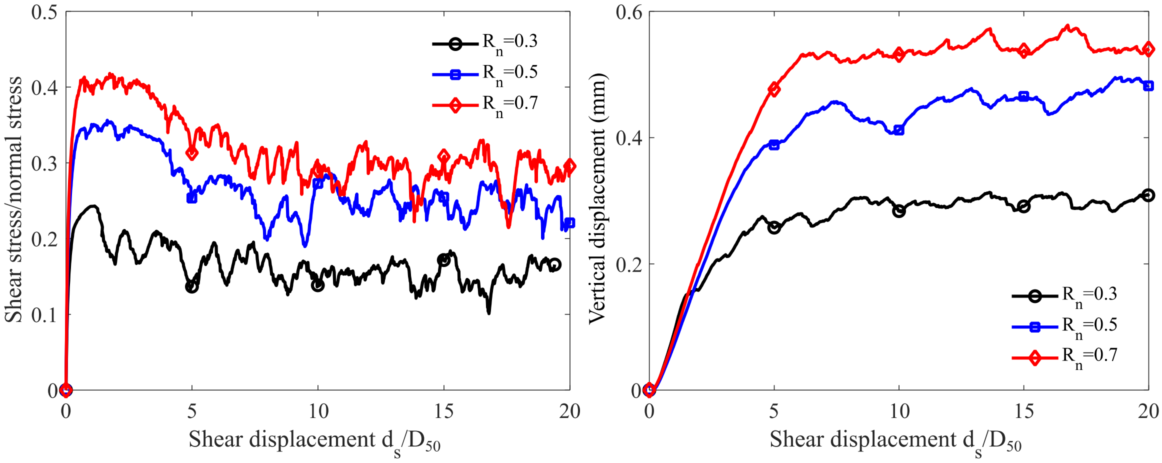

(a) **(b)**

Fig. 22 Effect of surface roughness on the shear stress/normal stress ratio (a) and the vertical displacement (b)

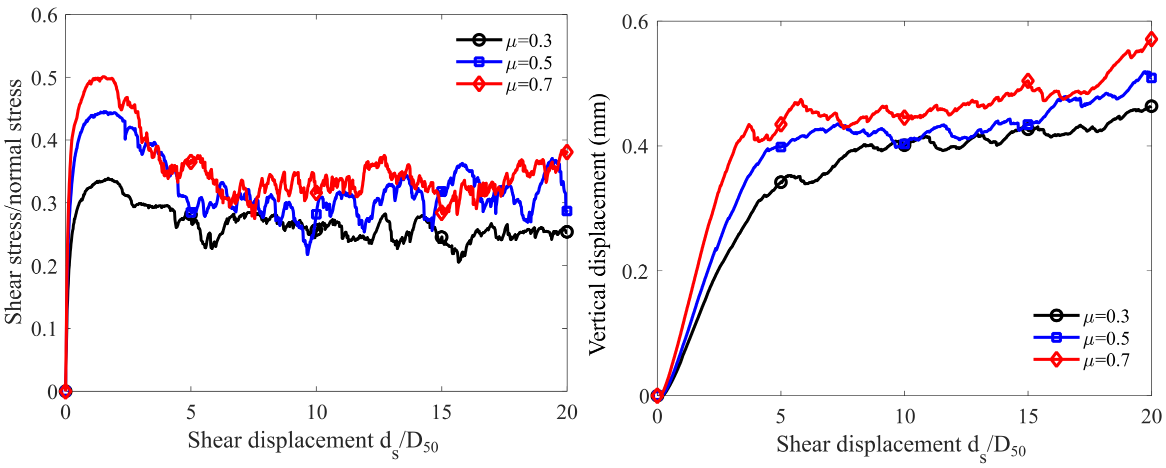

(a) **(b)**

Fig. 23 Effect of inter-particle friction coefficient on the shear stress/normal stress ratio (a) and the vertical displacement (b)

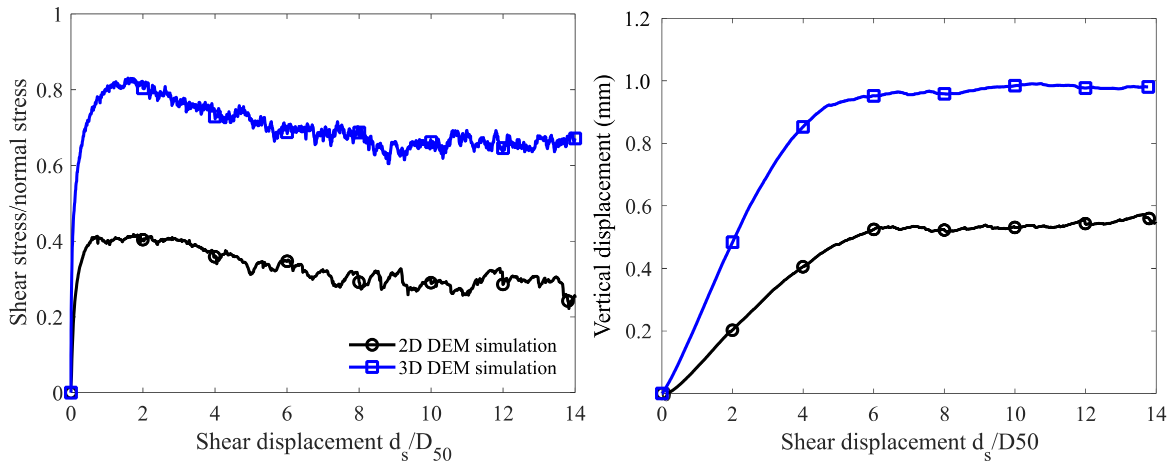

(a) **(b)**

Fig. 24 Comparison between 2D and 3D DEM simulations: (a) ratio of shear stress to normal stress versus shear displacement; and (b) vertical displacement versus shear displacement